Heavy Flavor and Quarkonium Production in pA Collisions

R. Vogt

Lawrence Livermore National Laboratory, Livermore, CA 94551, USA
Physics Department, University of California, Davis, CA 95616, USA

A Dependence of Open Charm and Quarkonium

Open charm appears to be independent of A ($N_{\rm bin}$) but note that the measurement is at midrapidity only

Definite A dependence for quarkonium while Drell-Yan is effectively independent of A

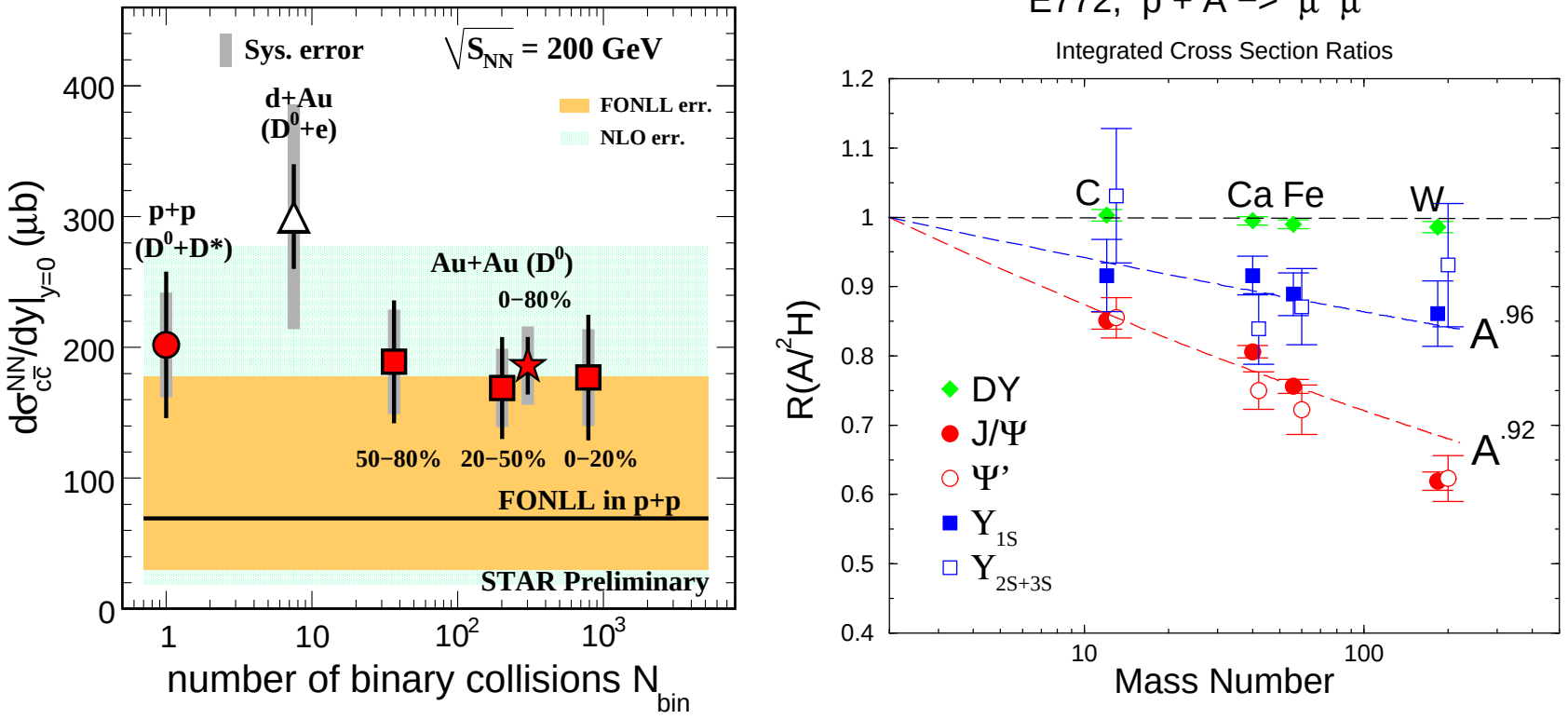

Figure 1: **(Left) The dependence of the open charm cross section on the number of binary collisions measured by the STAR Collaboration at central rapidity. (Right) The A dependence of quarkonium and Drell-Yan production measured by E772.**

E866 Measured Open Charm and J/ψ vs x_F

E866 also measured open charm pA dependence using single muons with $p_T^\mu > 1$ GeV/c (unpublished)

Different from J/ψ for $y < 0.7$ but similar for higher y, suggests that dominant effects are in the initial state

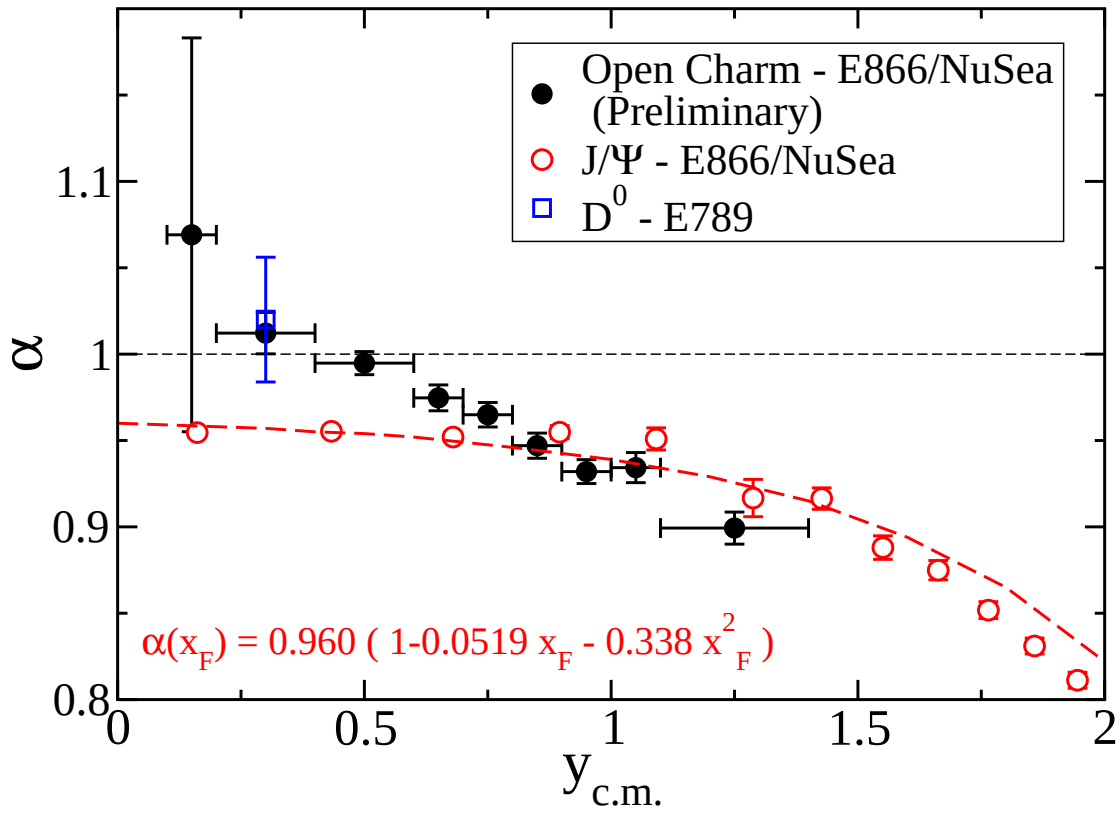

Figure 2: The J/ψ and open charm A dependence as a function of x_F (Mike Leitch).

Medium Effects Important with Nuclear Target

Nuclear effects often parameterized as

$$\sigma_{pA} = \sigma_{pp} A^{\alpha} \qquad \alpha(x_F, p_T)$$

For $\sqrt{s_{NN}} \leq 40$ GeV and $x_F > 0.25$, α decreases strongly with x_F – only low x_F effects probed by SPS and RHIC rapidity coverage

Possible cold matter effects

- **Nuclear Shadowing — initial-state effect on the parton distributions affecting total rate, important as a function of y/x_F**
- **Energy Loss — initial-state effect, elastic scatterings of projectile parton before hard scattering creating quarkonium state, need to study Drell-Yan production to get a handle on the strength when shadowing included**
- **Intrinsic Charm — initial-state effect, if light-cone models correct, should only contribute to forward production, assumed to have different A dependence than normal J/ψ production**
- **Absorption — final-state effect, after $c\overline{c}$ that forms the J/ψ has been produced, pair breaks up in matter due to interactions with nucleons**

Shadowing
DGLAP-style Evolution
Collinear Factorization

Parton Densities Modified in Nuclei

Nuclear deep-inelastic scattering measures quark modifications directly

More uncertainty in nuclear gluon distribution, only indirectly constrained by Q^2 evolution of parton densities

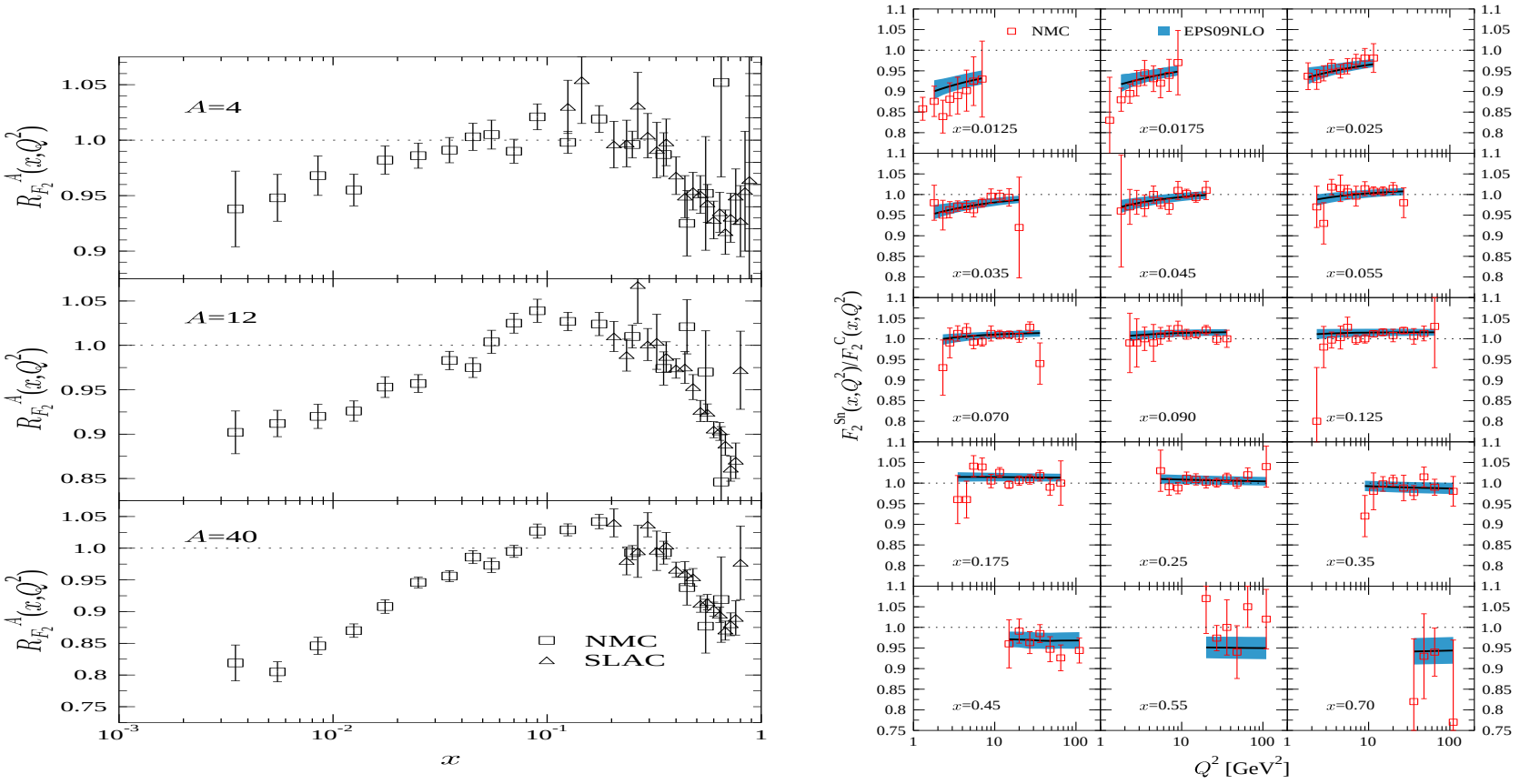

Figure 3: (Left) Ratios of charged parton densities in He, C, and Ca to D as a function of x. (Right) Evolution of gluon distributions in Sn relative to C targets with Q^2 for several fixed values of x. [From K.J. Eskola.]

Eskola *et al* Method: I

Other groups use different data sets, initial assumptions, but similar methods – all start with nDIS data, usually with a minimum factorization/renormalization scale of $\sim 1-2$ GeV^2

Nuclear effects on PDFs divided into x regions

- **shadowing; a depletion at $x \lesssim 0.1$,**
- **anti-shadowing; an excess at $0.1 \lesssim x \lesssim 0.3$,**
- **EMC effect; a depletion at $0.3 \lesssim x \lesssim 0.7$**
- **Fermi motion; an excess towards $x \to 1$ and beyond.**

Define ratios of the individual and total valence and sea quark distributions and the gluon ratio in nuclei relative to protons

$$
\begin{aligned}
R^A_{\bar{q}}(x,Q^2) &\equiv \frac{\bar{q}_A(x,Q^2)}{\bar{q}(x,Q^2)} \quad R^A_{q_V}(x,Q^2) \equiv \frac{q^A_V(x,Q^2)}{q_V(x,Q^2)} \quad R^A_G(x,Q^2) \equiv \frac{g^A(x,Q^2)}{g(x,Q^2)} \\
R^A_V(x,Q^2) &\equiv \frac{u^A_V(x,Q^2)+d^A_V(x,Q^2)}{u_V(x,Q^2)+d_V(x,Q^2)}, \\
R^A_S(x,Q^2) &\equiv \frac{\bar{u}_A(x,Q^2)+\bar{d}_A(x,Q^2)+\bar{s}_A(x,Q^2)}{\bar{u}(x,Q^2)+\bar{d}(x,Q^2)+\bar{s}(x,Q^2)}
\end{aligned}
$$

Most groups now have NLO sets and some include uncertainties, *e.g.* EPS09 includes 31 sets: 1 central + 30 obtained by varying each parameter by one standard deviation

Eskola *et al* Method: II

Determination of $R_i^A(x,Q^2)$ from nuclear deep-inelastic scattering (nDIS) and Drell-Yan (DY) data

- **Formulate $R_{F_2}^A(x,Q^2)$ and $R_{\rm DY}^A(x,Q^2)$ based on linear combinations of the quark and antiquark ratios**
- **Make an ansatz for $R_{F_2}^A(x,Q_0^2)$ based on nDIS data**
- **Decompose $R_{F_2}^A(x,Q_0^2)$ into R_V^A and R_S^A**
- **Constrain R_V^A using baryon number conservation**
  $\int_0^1 dx[u_V(x,Q_0^2)+d_V(x,Q_0^2)]R_V^A(x,Q_0^2) = \int_0^1 dx[u_V(x,Q_0^2)+d_V(x,Q_0^2)] = 3$
- **Constrain $R_G^A(x,Q_0^2)$ by momentum conservation (gluons removed at low x get put back at higher x, for stability of R_V^A and R_S^A assume gluon EMC effect)**
  $1 = \int_0^1 dx\, x\Big\{g(x,Q_0^2)R_G^A(x,Q_0^2)+[u_V(x,Q_0^2)+d_V(x,Q_0^2)]R_V^A(x,Q_0^2)+2[\bar{u}(x,Q_0^2)+\bar{d}(x,Q_0^2)+s(x,Q_0^2)]R_S^A(x,Q^2)\Big\}$
- **Perform DGLAP evolution of the initial nPDFs which can further constrain gluon shadowing**

$$\begin{aligned}\frac{\partial R_{F_2}^A(x,Q^2)}{\partial\log Q^2} &= \frac{\partial F_2^D(x,Q^2)/\partial\log Q^2}{F_2^D(x,Q^2)}\Big\{\frac{\partial F_2^A(x,Q^2)/\partial\log Q^2}{\partial F_2^D(x,Q^2)/\partial\log Q^2} - R_{F_2}^A(x,Q^2)\Big\}\\ &\approx \frac{5\alpha_s}{9\pi}\frac{xg(2x,Q^2)}{F_2^D(x,Q^2)}\Big\{R_G^A(2x,Q^2) - R_{F_2}^A(x,Q^2)\Big\}\end{aligned}$$

- **Constrain $R_S^A(x,Q_0^2)$ and $R_V^A(x,Q_0^2)$ with Drell-Yan data**
- **Repeat, repeat, repeat**

Comparison of LO and NLO nDS nPDFs

When data are available, LO and NLO shadowing results agree, as they are meant to by construction

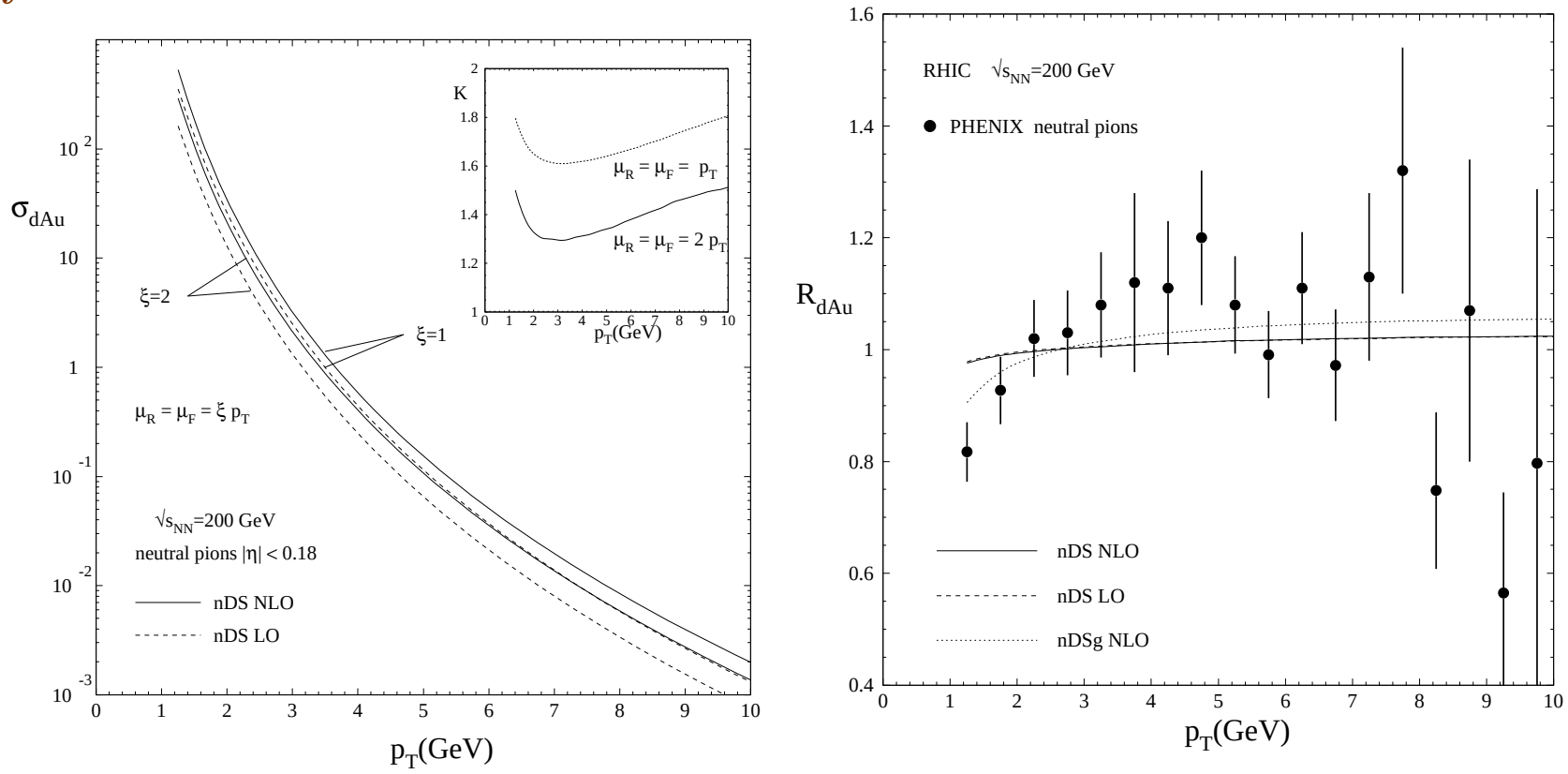

Figure 4: **(Left) The π^0 cross section in d+Au collisions at $\sqrt{s_{NN}} = 200$ GeV at LO and NLO. (Right) The LO and NLO calculations of $R_{\rm dAu}$, along with the NLO calculation with nDSg.**

Comparing Shadowing Parameterizations: x Dependence

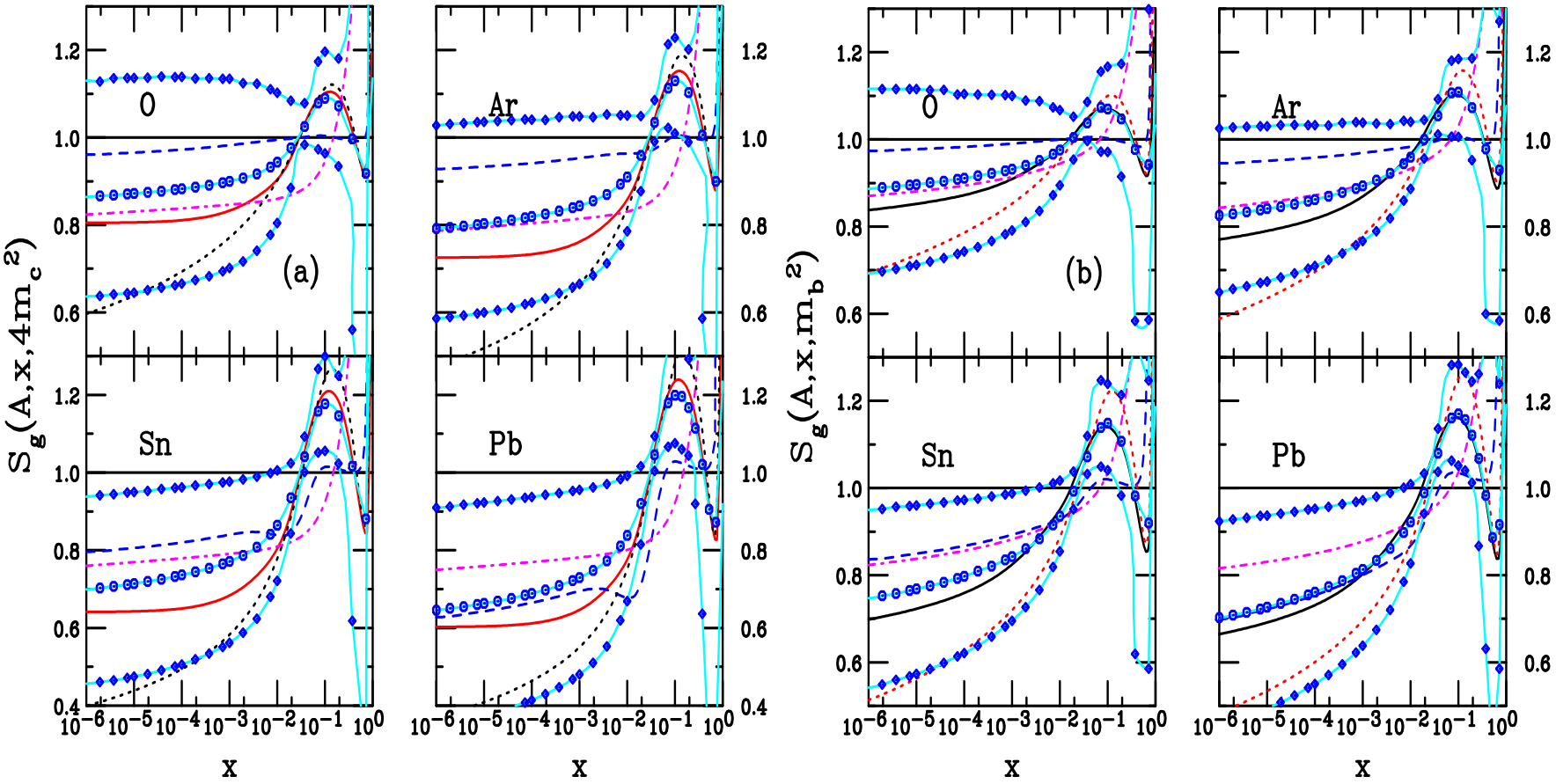

Figure 5: **Comparison of EKS98 (red), nDSg (blue), HKN (green), EPS08 (magenta), and EPS09 (cyan, with symbols) gluon shadowing parameterizations for J/ψ (left) and Υ (right) production scales with A =O, Ar, Sn and Pb.**

Saturation
Starting from the Nucleon
BFKL-type Evolution (Schematic Only)

Schematic View of Saturation Regime

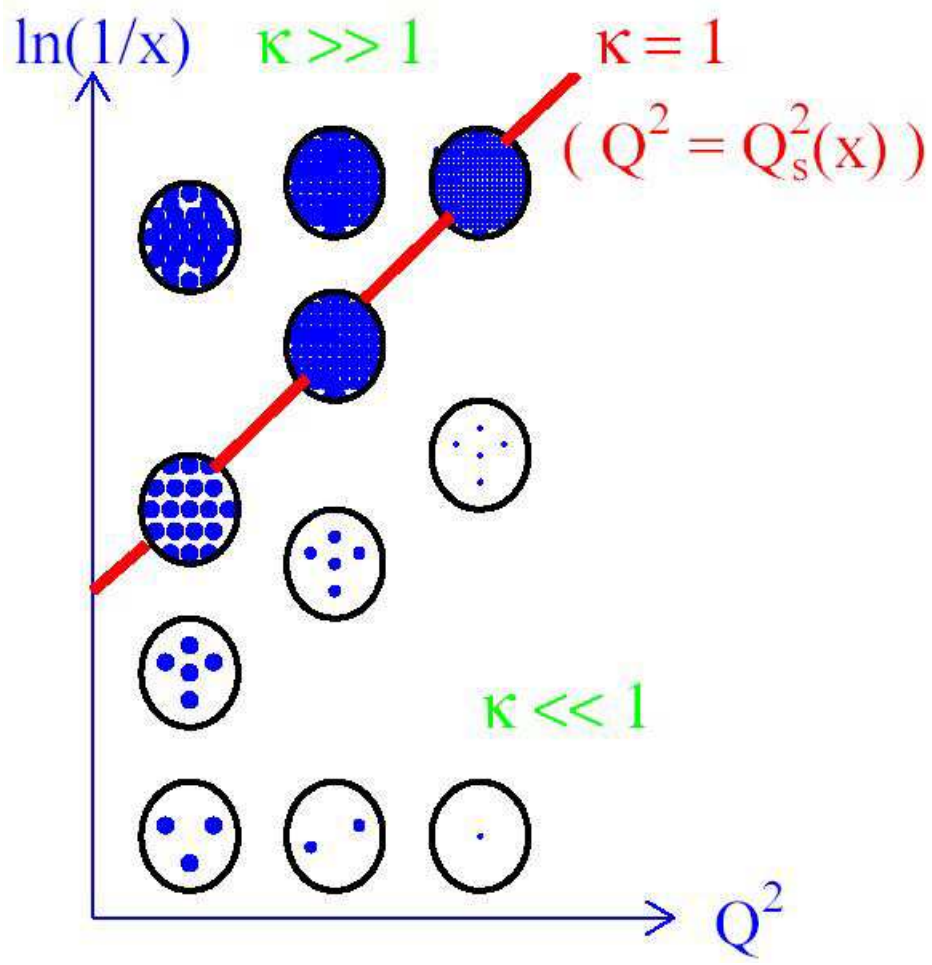

Saturation condition: when the gluon density, ρ_g, is sufficiently high, recombination of gluons $(2 \to 1)$ competes with emission of new partons $(1 \to 2)$ $\rho \sim 1/\alpha_s$

Packing factor: fraction of how much of nucleon/nuclear disk is packed with partons,
$\kappa = \sigma_{\rm dipole}/\pi R^2$, $\sigma_{\rm dipole} \propto F_2(x, Q^2)/Q^2$

$Q_{\rm sat}$ grows with increasing $\sqrt{s}$ and decreasing x

in nuclei $Q_{\rm sat}$ increases by $A^{1/3}$

Pinning Down the Gluon nPDF

To constrain gluon density using the J/ψ, also necessary to constrain other cold matter effects, left side shows NMC Sn/C J/ψ ratios, intermediate x only, not very conclusive

Right side: LO and NLO EPS09 shadowing ratios extracted from Q^2 evolution of nDIS; PHENIX π^0 data and momentum sum rules

LO ratios show wider antishadowing and bigger uncertainty in EMC region ($x > 0.3$), bigger uncertainty at low x

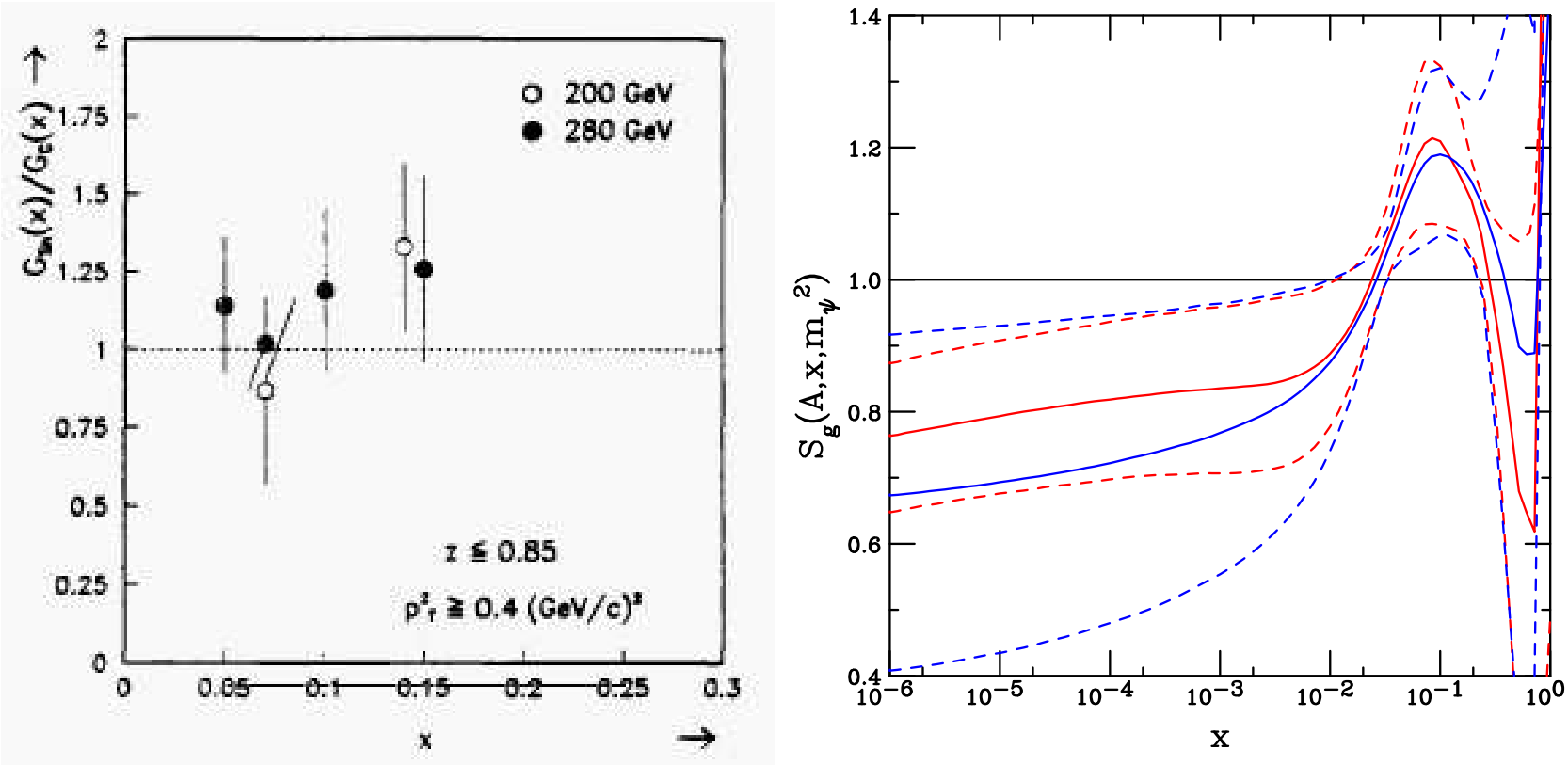

Figure 6: **(Left) Ratio of gluon distributions in Sn and C targets extracted from J/ψ production by NMC. (Right) The modification of the gluon densities at LO (blue) and NLO (red) with EPS09, including uncertainties (dashed lines), calculated at m_ψ.**

Shadowing on J/ψ in d+Au Collisions at $\sqrt{s_{NN}} = 200$ GeV

Left: $R_{\rm dAu}$ calculated at LO and NLO in CEM, Right: 'intrinsic' (LO CEM) vs. 'extrinsic' (LO CSM).

LO CEM calculation on left equivalent to 'intrinsic' $2 \to 1$ calculation with $p_T = 0$ on right-hand side

NLO CEM has higher average scale, shifts antishadowing peak to higher rapidity, and smaller scale dependence, similar to 'extrinsic' $2 \to 2$ LO CSM calculation

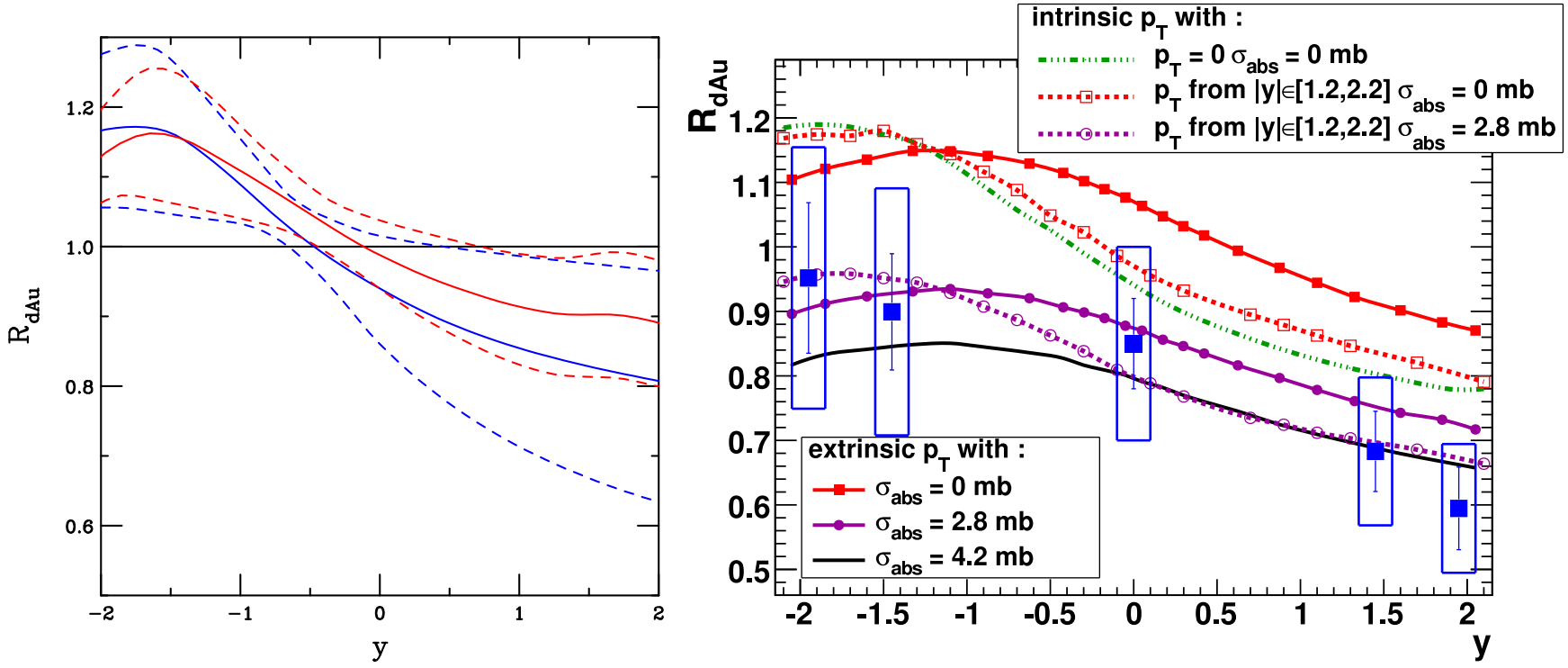

Figure 7: **Left: The LO and NLO calculations of $R_{\rm dAu}$. Right: 'Intrinsic' (CEM) vs. 'extrinsic' (CSM with s-channel cut) calculation of Ferreiro *et al.*.**

J/ψ A Dependence vs. x_2 and $y_{\rm cm}$

Effective α dissimilar as a function of x_2, closer to scaling for $y_{\rm cm}$

At negative x_F, the HERA-B result suggests a neglible effective J/ψ absorption crosss section

Argument for more physics at forward x_F than accounted for by nuclear shadowing

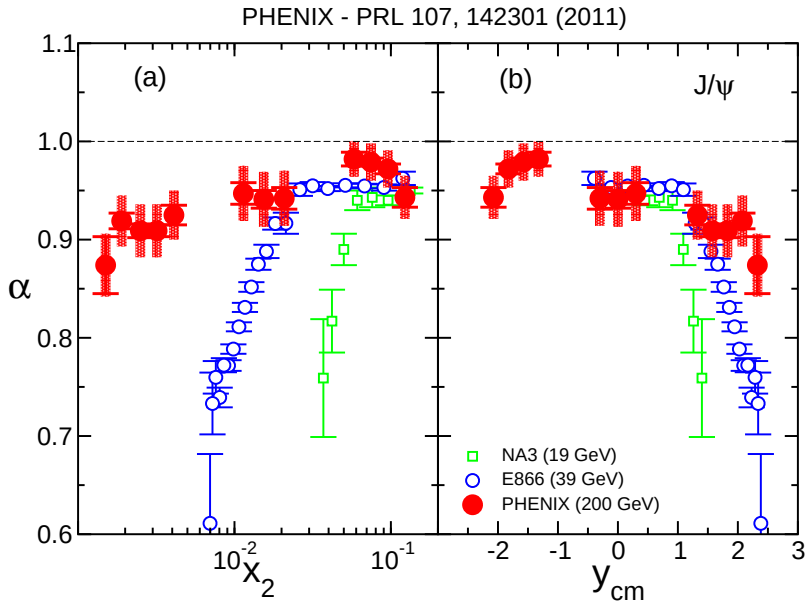

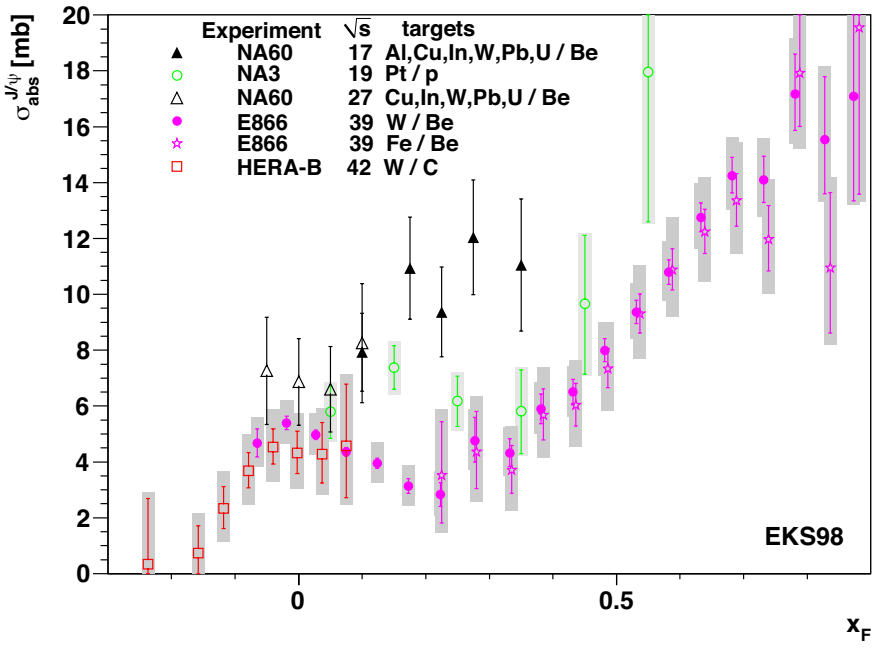

Figure 8: (Left) Comparison of effective α for NA3, E866 and PHENIX. (Mike Leitch) (Right) Comparison of effective $\sigma_{\rm abs}$ for J/ψ (from QWG report, 2010).

Energy-Loss Models
Drell-Yan
J/ψ

Drell-Yan Production: Simplest Case

Good theory for pp production, small K factor with NLO calculation

$K = 1.124 \pm 0.007$, $\chi^2/\mathrm{ndf} = 1.4$ relative to E866 measurements in 800 GeV pp collisions (J.C. Webb Ph.D. thesis [arXiv:hep-ex/0302019]).

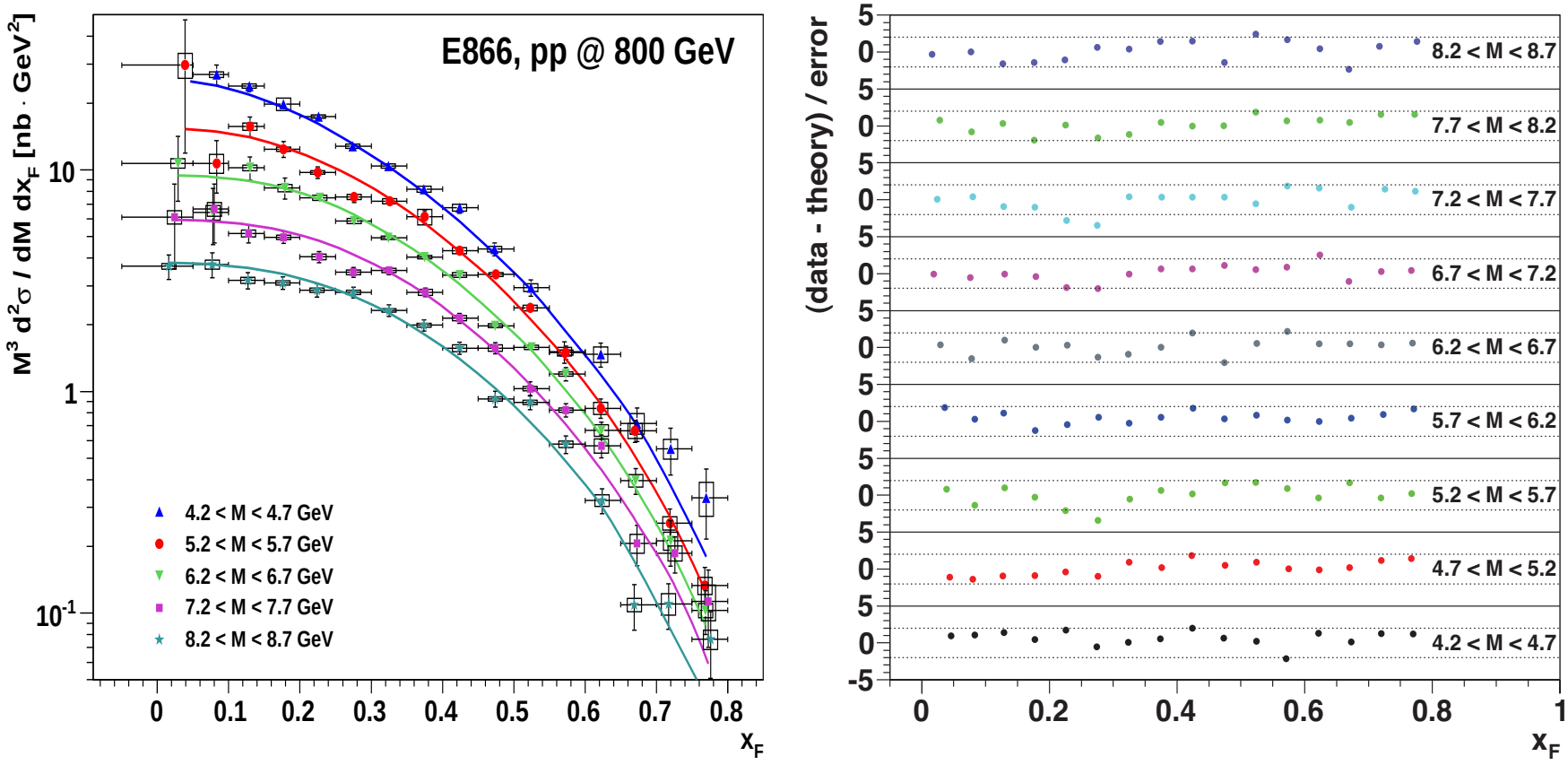

Figure 9: Left: The x_F dependence of the Drell-Yan cross section in several mass bins from 800 GeV pp colisions compared to NLO calculations. Right: Difference between the measured Drell-Yan cross section and the NLO calculations in the same mass bin.

Energy Loss in Drell-Yan? NA3 p+Pt at 400 GeV

Compare NA3 data with NLO calculations with/without central EPS09 nPDFs (difference small)

Test parameterization of initial state energy loss

$$x_1' = x_1(1-\epsilon_q)^{N-1}$$

x_1' enters $M^2 = x_1' x_2 s_{_{NN}}$, x_1 is in nPDFs, N is number of NN collisions, $\propto A^{1/3}$

Vary ϵ_q to get best fit, 99% confidence level gives upper limit on ϵ_q of 0.0020

Assume $\epsilon_g = (9/4)\epsilon_q$ for NLO qg contribution

$K \sim 1$, χ^2/ndf slightly smaller with no shadowing

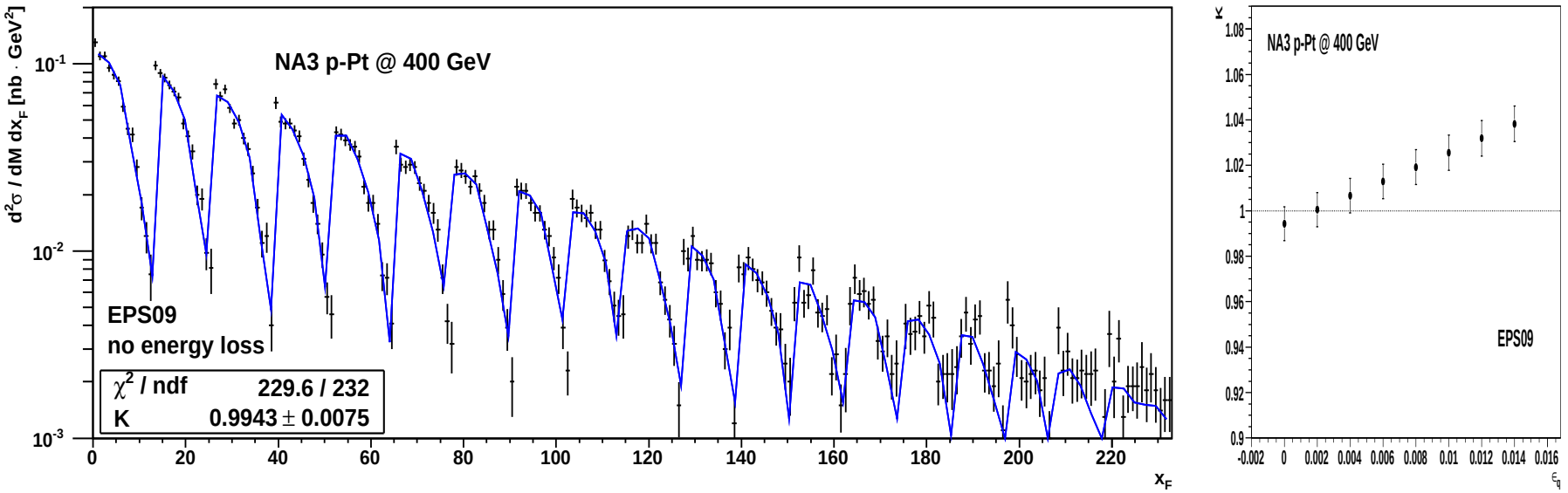

Figure 10: Left: The invariant DY cross section in pPt collisions at 400 GeV as a function of x_F in different mass bins with EPS09 nPDFs. Right: The K factors found in comparison to the data with various values of the energy loss parameter ϵ_q.

Is Shadowing Sufficient to Explain Data?

Extracting energy loss from shadowing difficult, the two are intertwined

At 400 GeV and $4 < M < 9$ GeV, the modification of the Drell-Yan cross section is nearly independent of x_F, thus energy loss extracted from data is basically independent of EPS09 PDFs; average K factor shift can account for difference

E866 W/Be and Fe/Be ratios at 800 GeV in similar mass regions suggest energy loss parameter no larger than that found at 400 GeV; E772 W/D and Fe/D ratios confirm trend

Is energy loss a predominantly final-state effect? Then Drell-Yan is unaffected...

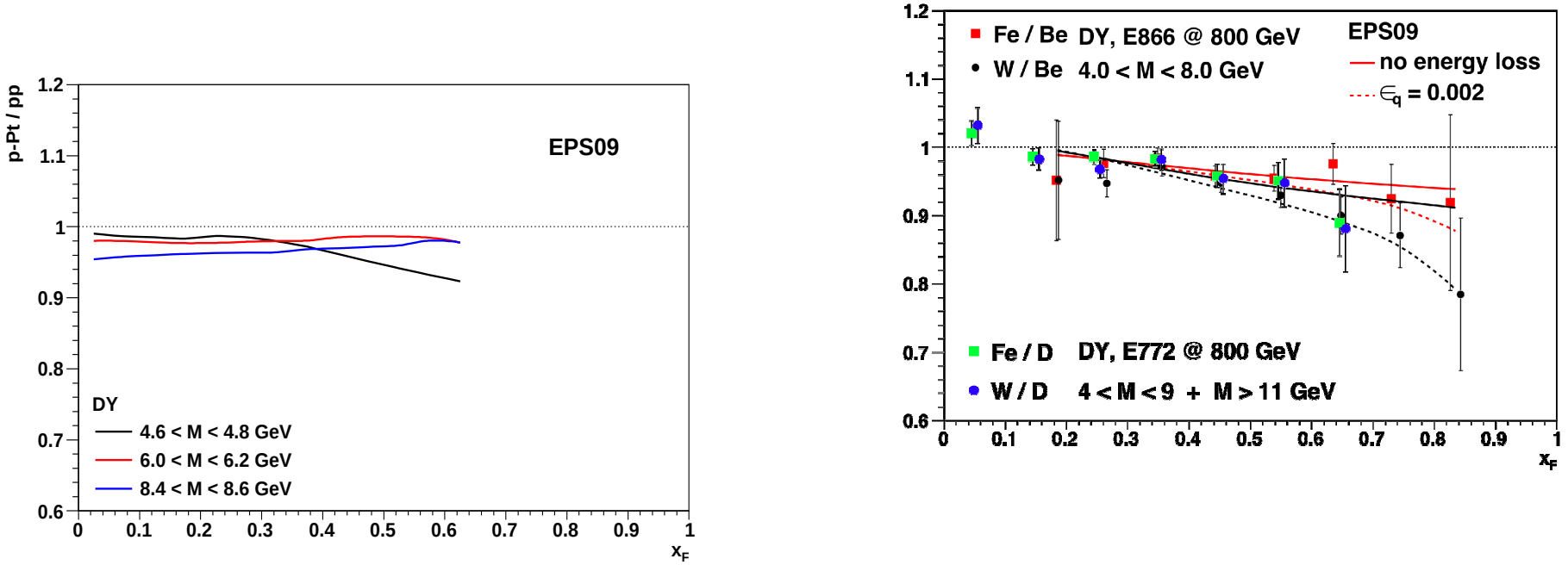

Figure 11: Left: The 400 GeV pPt/pp ratio for Drell-Yan production in several different mass bins as a function of x_F with the central EPS09 nPDF. Right: Heavy-to-light ratios for Drell-Yan production at 800 GeV. The curves show the EPS09 results with no energy loss included (solid) and $\epsilon_q = 0.0020$ (dashed) the same value obtained at 400 GeV. The Fe/Be ratio, similar to Fe/D, is shown in red while the W/Be (W/D) ratios are shown in black. (Note that these curves

Other DY Energy Loss Calculations

Left-hand side shows limits on energy loss in different cases (fitting schematic parameters k_1, k_2 and k_3 to E866 DY data):

Gavin and Milana (PRL 68, 1834 (1992)), $\Delta x_1 = -k_1 x_1 A^{1/3}$

Brodsky and Hoyer (PL B 298, 165 (1993)), $\Delta x_1 = -(k_2/s)A^{1/3}$

Baier *et al* **(NP B 484, 265 (1997); 531, 403 (1998)),** $\Delta x_1 = -(k_3/s)A^{2/3}$

Right-hand side is calculation by Kopeliovich *et al* **(PRL 86, 4483 (2001)),** $dE/dx = 2.32 \pm 0.52 \pm 0.50$ **GeV/fm fit to E772 data**

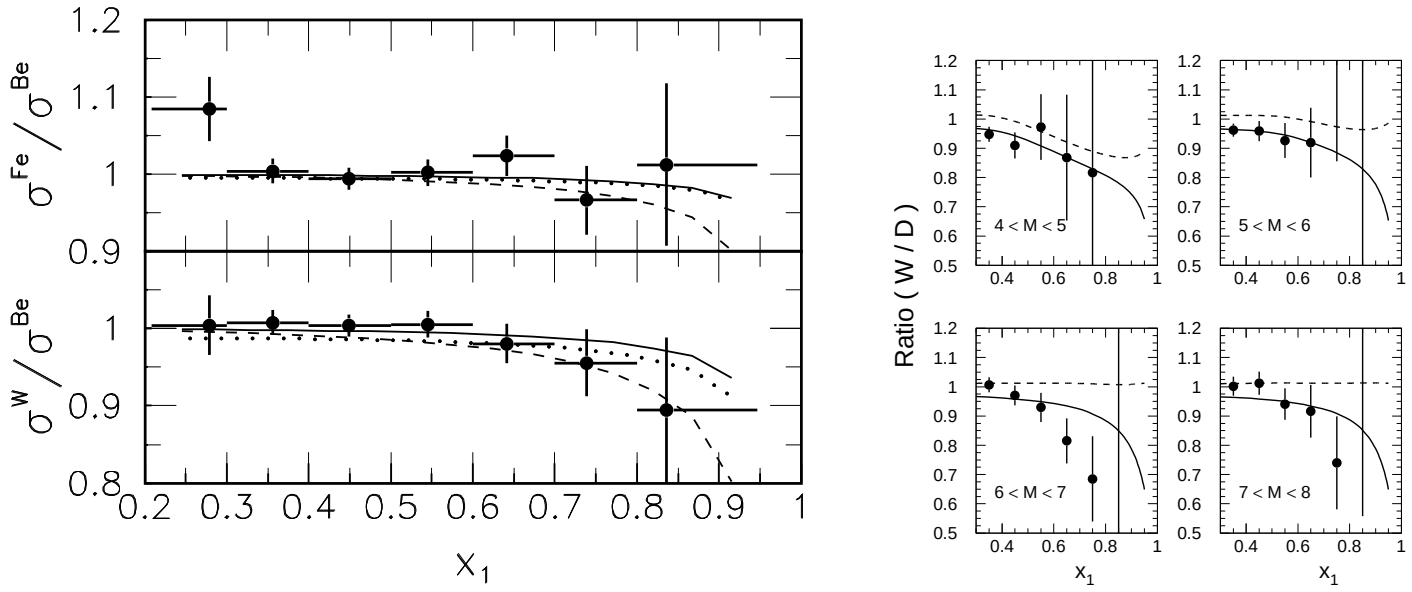

Figure 12: Left: Cross section ratios, Fe/Be and W/Be, calculated with energy loss, after E866 data correction for EKS98 shadowing. The dashed curve is the Gavin-Milana best fit while the dashed curve is the 1σ limit. The dotted curve is the upper limit on energy loss for the results with $\Delta x_1 \propto 1/s$. Right: Calculation of W/D ratio for a specific E772 mass bin, shadowing and energy loss are included in the result.

Adding Initial State Energy Loss to J/ψ Production

Rather large EPS09 uncertainty reduced in ratios; clearly initial-state shadowing is insufficient to describe effect

Combination of shadowing and energy loss with relatively x_F-independent absorption compares relatively well with the data for $x_F > 0.2$; HOWEVER, the assumed ϵ_g is much larger than ϵ_q for Drell-Yan production – final-state loss?? Stronger absorption closer to target? Formation time effects not included

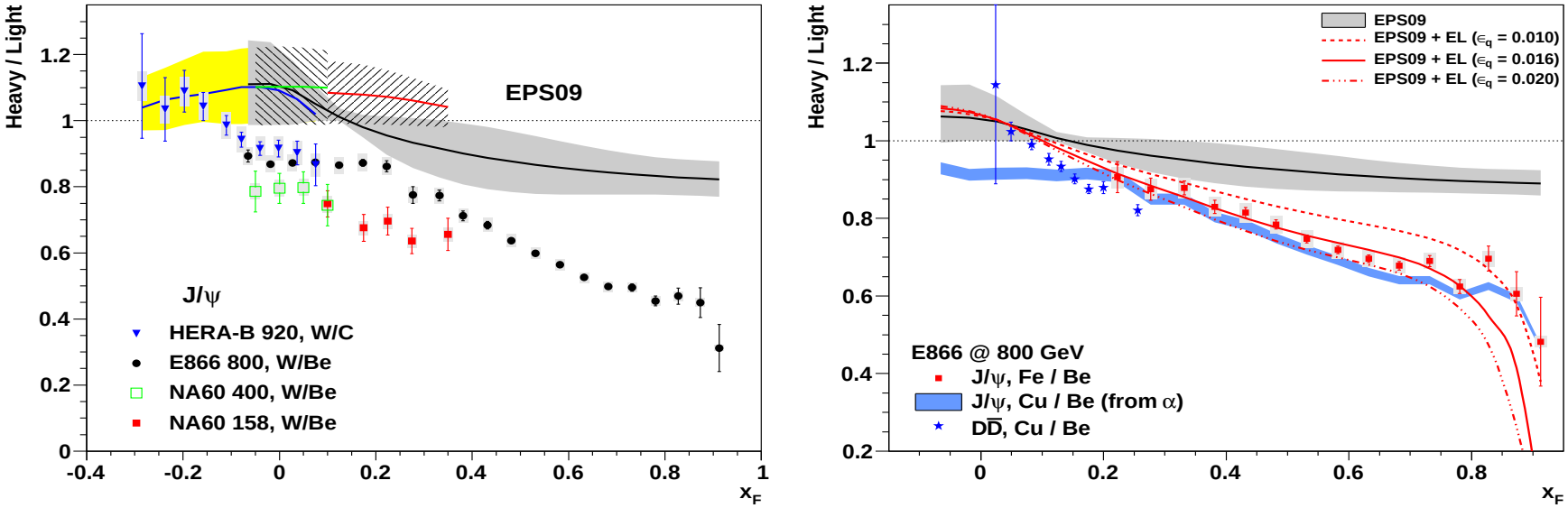

Figure 13: Left: The heavy to light ratios for W/Be in fixed target interactions. Right: Convolution of shadowing, absorption and various strengths of initial-state energy loss by quarks compared to the E866 data.

Initial-State Energy Loss with HERA-B Data (RV)

HERA-B 2008 data compared to E866 and calculations with initial-state energy loss similar to those done for Drell-Yan by E866 but no fitting done to E866 data, only using original parameters

Final HERA-B data do show some rise at negative x_F

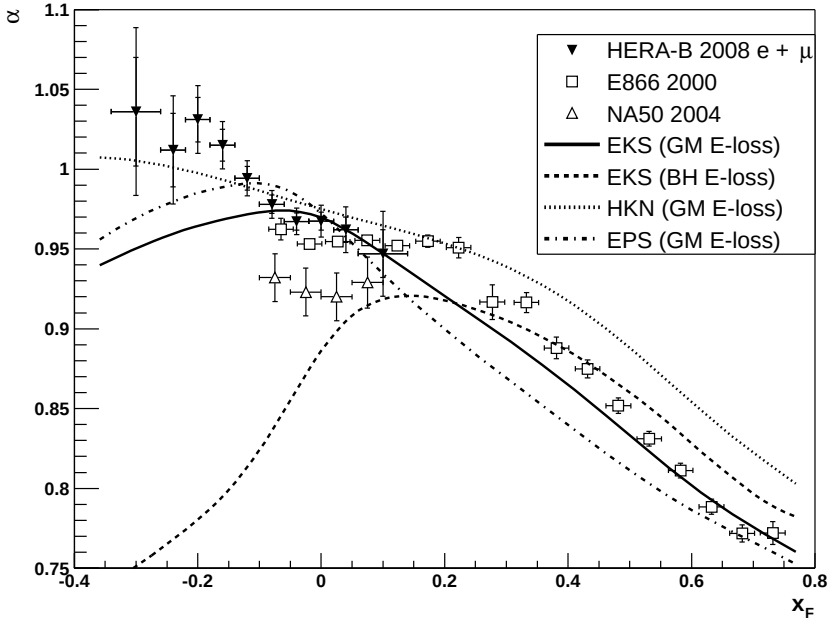

Figure 14: Measurements of α as a function of x_F by HERA-B (filled triangles, plotted with total and statistical uncertainties), E866 ($\sqrt{s} = 38.8\,\text{GeV}$) (empty squares) and NA50 ($\sqrt{s} = 29.0\,\text{GeV}$) (empty triangles). The curves were calculated by RV based on three different nuclear parton distribution functions: (EPS08, EKS98 and HKN) and two models of initial state energy-loss: Gavin & Milana and Brodsky & Hoyer. For all approaches, energy loss, intrinsic charm and shadowing are taken into account.

Final-State Energy Loss (Kharzeev and Satz)

Backward rise could be due to final-state energy loss

Kharzeev and Satz (Z. Phys. C 60, 389 (1993)), assumed final-state loss of color octet $c\bar{c}$, momentum is reduced by $\sim \kappa L_A$ where κ is string tension and L_A is path length, ψ state produced with x_F/δ where $\delta \approx 1 - \kappa L_A/P_\psi$

$$G_A(x_F) \propto S_A G_p(x_F) + (1 - S_A)\frac{G_p(x_F/\delta)}{\delta}\theta(1 - x_F/\delta)$$

Lower energies show a stronger decrease

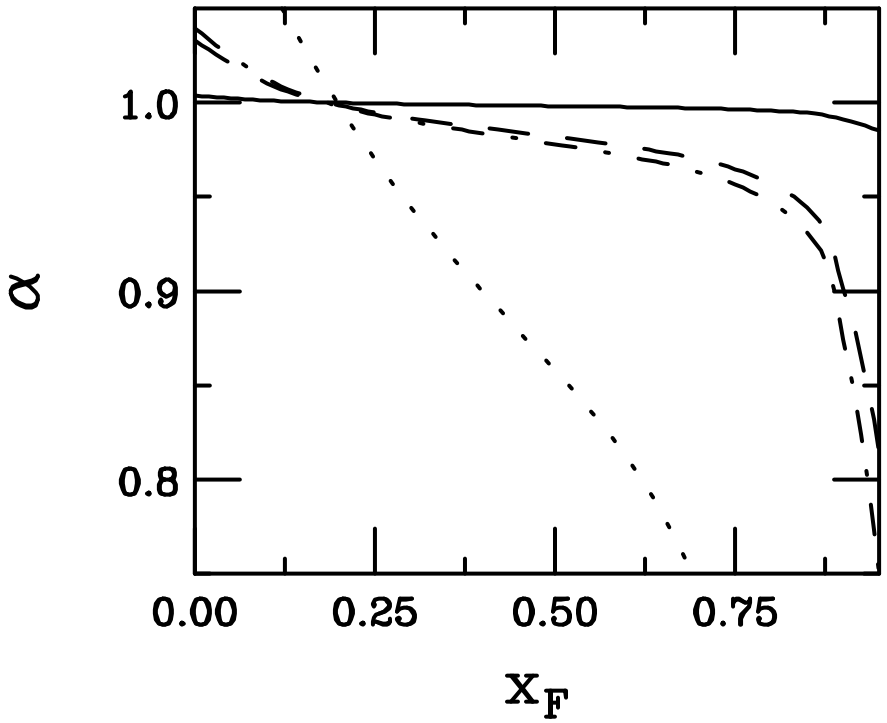

Figure 15: The A dependence of ψ production assuming KS loss for $x_F > 0$. Octet cross sections of 1 mb (solid), 20 mb (dashed) and 40 mb (dot-dashed) are calculated with the MRST LO parton densities at 800 GeV. At 120 GeV, a 40 mb octet cross section is assumed (dotted).

Final-State Energy Loss (Arleo and Peigne)

Arleo and Peigne (arXiv:1204.4609) fits an energy loss parameter that also depends on L_A to E866 data and uses the same parameter for other energies

They find a somewhat better fit assuming gluon saturation, with a modified energy loss parameter and see a strong $\sqrt{s}$ dependence

$$\frac{1}{A}\frac{d\sigma_{pA}(x_F)}{dx_F} = \int_0^{E_p-E} d\epsilon P(\epsilon)\frac{d\sigma_{pp}(x_F+\delta x_F(\epsilon))}{dx_F}$$

Backward x_F effect is large for this scenario

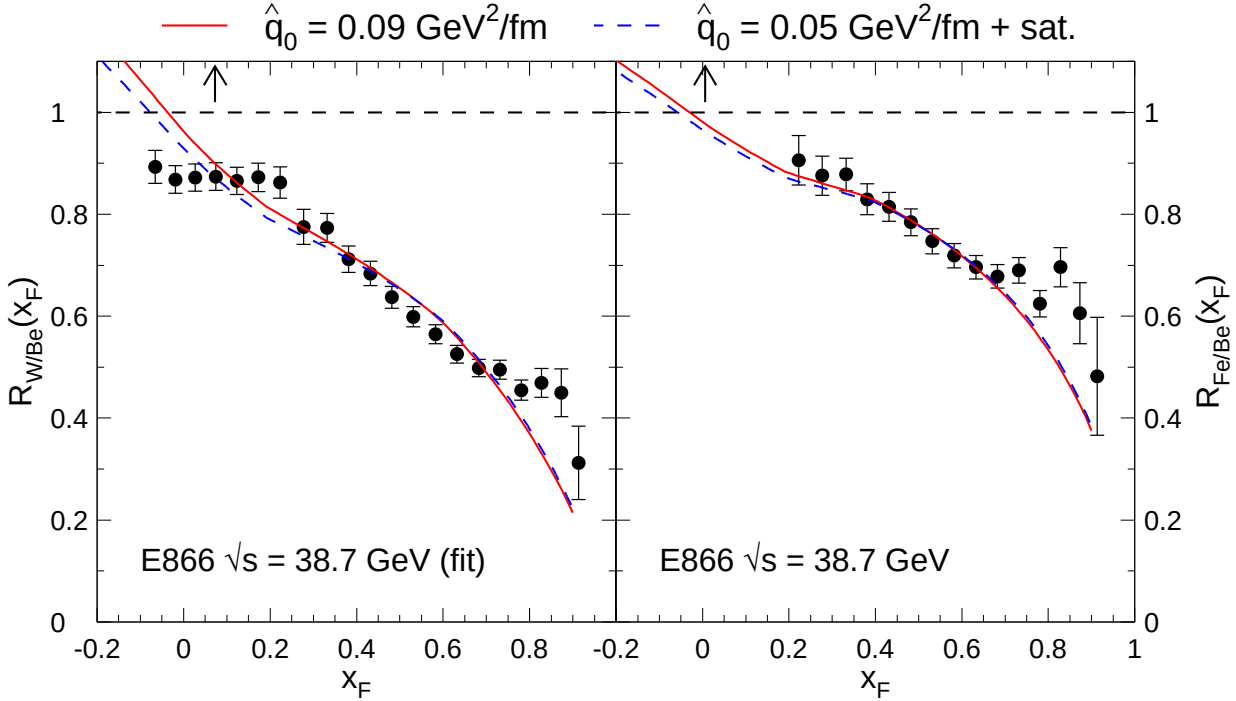

Figure 16: E866 J/ψ suppression in pW (left) and pFe (right) collisions calculated by Arleo and Peigne.

Intrinsic Charm

Intrinsic Charm

Proton wavefunction can be expanded as sum over complete basis of quark and gluon states: $|\Psi_p\rangle = \Sigma_m |m\rangle \, \psi_{m/p}(x_i, k_{T,i}, \lambda_i)$

$|m\rangle$ are color singlet state fluctuations into Fock components $|uud\rangle$, $|uudg\rangle \cdots |uudc\overline{c}\rangle$

Boost invariant wavefunctions $\psi_{m/p}(x_i, k_{T,i}, \lambda_i)$ depend on $x_i = k_i^+/P^+$ and $k_{T,i}$ the momentum fraction and transverse momentum for each parton. Momentum conservation demands $\Sigma_{i=1}^n x_i = 1$ and $\Sigma_{i=1}^n \vec{k}_{T,i} = 0$, where n is the number of partons in Fock state $|m\rangle$

The intrinsic charm fluctuations can be freed by a soft interaction if the system is probed during the time $\Delta t = 2p_{\rm lab}/M^2_{c\overline{c}}$ that the fluctuations exist

Dominant Fock state configurations have minimal invariant mass, $M^2 = \Sigma_i \, m^2_{T,i}/x_i$, where $m^2_{T,i} = k^2_{T,i} + m^2_i$ is the squared transverse mass of parton i in the state; corresponds to configurations with equal rapidity constituents

Since intrinsic charm quarks have the same rapidity as other partons in the state, their larger mass gives them a higher momentum fraction than the comoving light partons

Light Cone Intrinsic Charm Quark Distribution

Frame-independent Fock state wavefunction

$$\Psi(\vec{k}_{\perp i}, x_i) = \frac{\Gamma(\vec{k}_{\perp i}, x_i)}{m_h^2 - M^2}$$

Vertex function Γ assumed to be slowly varying so the denominator controls the particle distributions; mean k_T^2 used to calculate the x distributions

Probability distribution for n-particle Fock state as a function of x

$$\frac{dP_{\rm ic}}{dx_i \cdots dx_n} = N_n[\alpha_s^2(M_{c\overline{c}})]^2 \; \frac{\delta(1 - \Sigma_{i=1}^n x_i)}{(m_h^2 - \Sigma_{i=1}^n (\widehat{m}_i^2/x_i))^2}$$

N_n is a normalization to total probability for each state; heavy quark limit, $\widehat{m}_c$, $\widehat{m}_{\overline{c}} \gg m_h$, $\widehat{m}_q$

$$\frac{dP_{\rm ic}}{dx_i \cdots dx_n} = N_n[\alpha_s^2(M_{c\overline{c}})]^2 \frac{x_c x_{\overline{c}}}{(x_c + x_{\overline{c}})^2} \; \delta(1 - \sum_{i=1}^n x_i)$$

Finally, in a $|uudc\overline{c}\rangle$ state, $n = 5$ and integration over light quarks and $\overline{c}$ gives

$$c(x) \propto \frac{dP_{\rm ic}(x)}{dx} = \frac{1}{2} N_5 x^2 [\frac{1}{3}(1-x)(1 + 10x + x^2) + 2x(1+x)\ln x]$$

If the intrinsic charm probability is 1%, $N_5 = 36$

Intrinsic Charm Structure Functions

Simplest LO F_2^c, no mass effects $F_2^{(0)}(x) = \frac{8}{9} x c(x)$

Hoffmann and Moore incorporated mass effects: scaling variable, $\xi = 2ax[1 + (1 + 4\rho x^2)^{1/2}]^{-1}$ **where** $\rho = m_p^2/Q^2$, $a = [(1 + 4\lambda)^{1/2} + 1]/2$ **and** $\lambda = m_c^2/Q^2$, $c\overline{c}$ **mass constraint,** $\xi \leq \gamma < 1$, $\gamma = 2a\hat{x}[1 + (1 + 4\rho\hat{x}^2)^{1/2}]^{-1}$ $[c(z, \gamma) = c(z) - zc(\gamma)/\gamma$ **for** $z \leq \gamma$**; 0 otherwise]**

$$F_2^{(0)}(x, Q^2, m_c^2) = \frac{8}{9}\xi c(\xi, \gamma)$$

Generalized operator product expansion to include m_c, m_p **for final LO result**

$$\begin{aligned} F_2^{(0)}(x, Q^2, m_c^2) &= \frac{8x^2}{9(1 + 4\rho x^2)^{3/2}} \left[\frac{(1 + 4\lambda)}{\xi} c(\xi, \gamma) + 3\hat{g}(\xi, \gamma) \right] \\ \hat{g}(\xi, \gamma) &= \frac{2\rho x}{(1 + 4\rho x^2)} \int_\xi^\gamma dt \frac{c(t, \gamma)}{t} \left(1 - \frac{\lambda}{\rho t^2} \right) \left[1 + 2\rho x t + \frac{2\lambda x}{t} \right] \end{aligned}$$

The NLO component of intrinsic F_2^c **is**

$$F_2^{(1)}(x, Q^2, m_c^2) = \frac{8}{9}\xi \int_{\xi/\gamma}^1 \frac{dz}{z} c(\xi/z, \gamma) \sigma_2^{(1)}(z, \lambda)$$

$$\begin{aligned} \sigma_2^{(1)}(z, \lambda) = \frac{2\alpha_s}{3\pi}\delta(1 - z)\Big\{ & 4\ln\lambda - 2 + \sqrt{1 + 4\lambda} L + \frac{(1 + 2\lambda)}{\sqrt{1 + 4\lambda}} [3L^2 + 4L + 4\mathrm{Li}_2(-d/a) + 2L\ln\lambda - 4L\ln(1 + 4\lambda) + 2\mathrm{Li}_2(d^2/a^2)] \Big\} + \frac{\alpha_s}{3\pi} \frac{1}{(1 + 4\lambda z^2)^2} \\ \times \Big\{ & \frac{1}{[1 - (1 - \lambda)z]^2} [(1 - z)(1 - 2z - 6z^2 + 8z^4) + 6\lambda z(1 - z)(3 - 15z - 2z^2 + 8z^3) + 4\lambda^2 z^2 (8 - 77z + 65z^2 - 2z^3) + 16\lambda^3 z^3 (1 - 21z + 12z^2) \\ & - 128\lambda^4 z^5] - \frac{2\hat{L}}{\sqrt{1 + 4\lambda z^2}} [(1 + z)(1 + 2z^2) - 2\lambda z(2 - 11z - 11z^2) - 8\lambda^2 z^2 (1 - 9z)] - \frac{8z^4(1 + 4\lambda)^2}{(1 - z)_+} - \frac{4z^4(1 + 2\lambda)(1 + 4\lambda)^2 \hat{L}}{\sqrt{1 + 4\lambda z^2}(1 - z)_+} \Big\} \end{aligned}$$

$$\hat{L} = \ln \left[\frac{4\lambda z[1 - (1 - \lambda)z]}{(1 + 2\lambda z + \sqrt{1 + 4\lambda z^2})^2} \right]$$

Intrinsic F_2^c for EMC Analysis

IC contribution at higher Q^2 and x than EC, NLO range is not as broad as LO

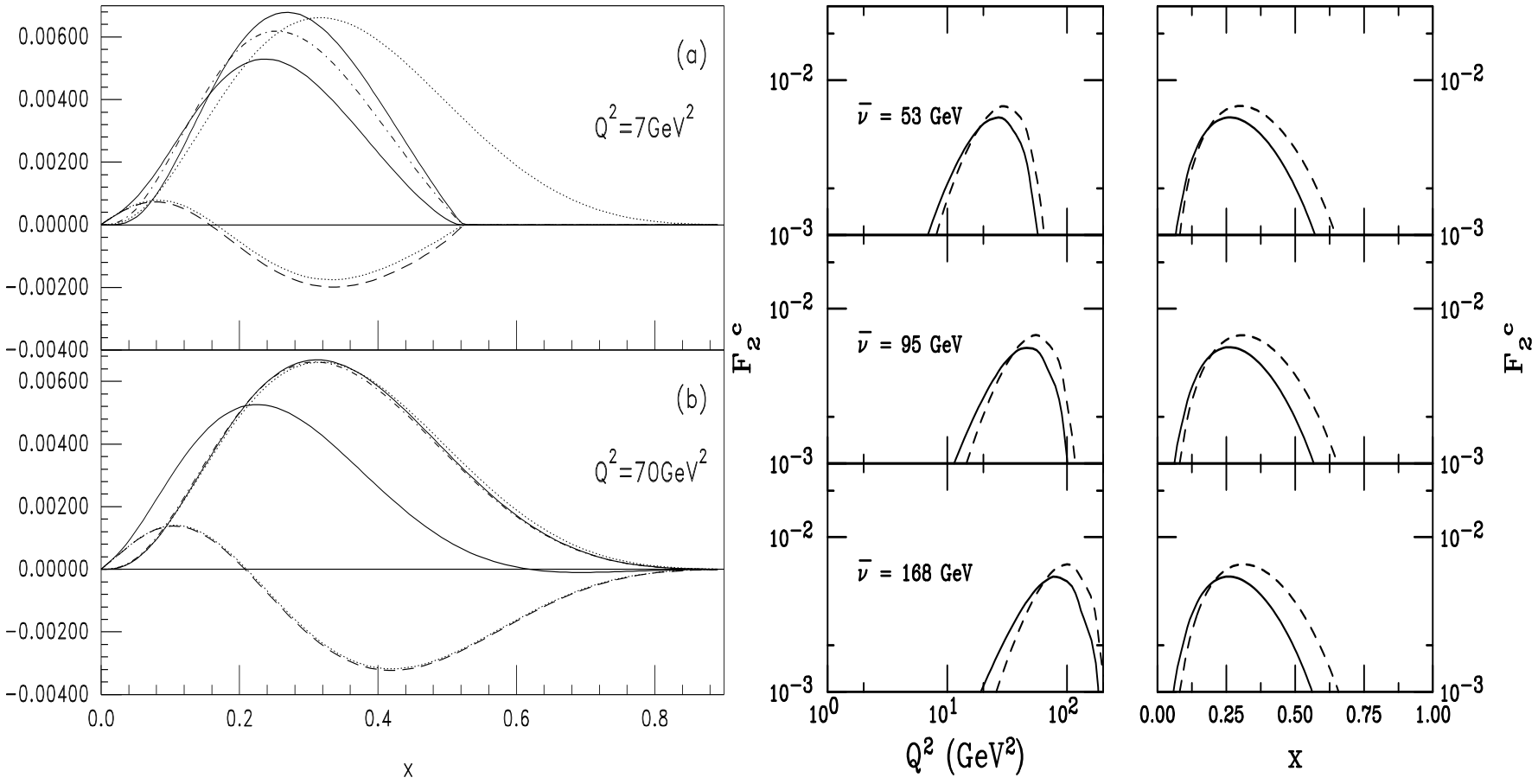

Figure 17: (Left) The IC contributions to the structure function $F_2(x, Q^2, m_c^2)$. At LO we show the massless result (upper dotted), the ξ-scaling result (dot-dashed) and the full kinematically corrected formula (upper solid). The full NLO correction (lower dotted) and the leading-log approximation (dashed) are also shown, along with the sum of the LO and NLO full results (lower solid). The results are given for $Q^2 = 7$ (a) and 70 (b) GeV^2. From Harris, Smith and RV. (Right) The intrinsic charm structure function used in the EMC analysis as a function of Q^2 (left-hand side) and x (right-hand side). From top to bottom the average energy transfer ν is 53, 95 and 168 GeV respectively. The full LO (dashed) and NLO (solid) results are shown.

Extrinsic Charm $(\gamma^*(q) + a_1(k_1) \to c(p_1) + \overline{c}(p_2) + a_2(k_2))$

Structure function

$$F_2(x,Q^2,m_c^2) = \frac{Q^2\alpha_s(\mu^2)}{4\pi^2 m_c^2}\int_{\xi_{\min}}^1 \frac{d\xi}{\xi}\left[e_c^2 f_{g/p}(\xi,\mu^2)c_{2,g}^{(0)}\right] \frac{Q^2\alpha_s^2(\mu^2)}{\pi m_c^2}\int_{\xi_{\min}}^1 \frac{d\xi}{\xi}\left\{e_c^2 f_{g/p}(\xi,\mu_c^2)\left(c_{2,g}^{(1)} + \overline{c}_{2,g}^{(1)}\ln\frac{\mu^2}{m_c^2}\right)\right.$$
$$\left. + \sum_{i=q,\overline{q}} f_{i/p}(\xi,\mu^2)\left[e_c^2\left(c_{2,i}^{(1)} + \overline{c}_{2,i}^{(1)}\ln\frac{\mu^2}{m_c^2}\right) e_i^2\, d_{2,i}^{(1)} + e_c\, e_i\, o_{2,i}^{(1)}\right]\right\}$$

$\xi_{\min} = x(4m_c^2+Q^2)/Q^2$; c_i, d_i and o_i are scale-independent coefficient functions: c_i is for $\gamma^* c$ coupling, d_i for $\gamma^* q$ coupling, o is interference term

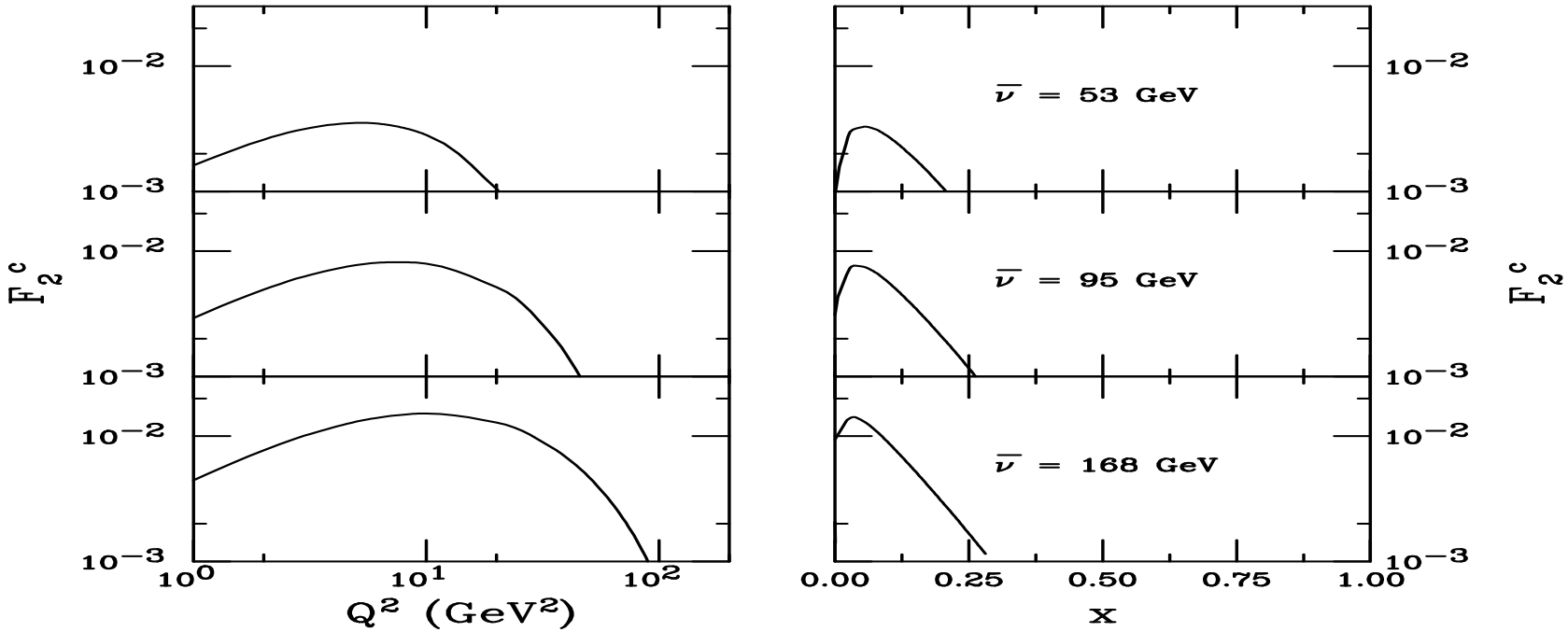

Figure 18: The extrinsic charm structure function used in the EMC analysis as a function of Q^2 (left-hand side) and x (right-hand side) calculated with $m_c = 1.5$ GeV, $\mu^2 = Q^2 + 20\,\mathrm{GeV}^2$ and CTEQ3 in the $\overline{\mathrm{MS}}$ scheme. From top to bottom the average energy transfer ν is 53, 95 and 168 GeV respectively.

Comparison to EMC Data

Normalization of EC and IC components free parameters in fit to EMC charm data (Harris, Smith and RV) – note old PDFs used in analysis

$$F_2^c(x,Q^2,m_c^2) = \alpha\, F_2^{c,\mathrm{EC}}(x,Q^2,m_c^2) + \beta\, F_2^{c,\mathrm{IC}}(x,Q^2,m_c^2)$$

α gives measure of NNLO correction, β is based on a 1% IC normalization

Uncertainties are for 95% confidence level; most significant result is at highest $\overline{\nu}$

	$\bar{\nu} = 53$ GeV		$\bar{\nu} = 95$ GeV		$\bar{\nu} = 168$ GeV	
PDF	α	β	α	β	α	β
CTEQ3	0.95 ± 0.64	0.36 ± 0.58	1.20 ± 0.13	0.39 ± 0.31	1.27 ± 0.06	0.92 ± 0.53
MRS G	1.02 ± 0.69	0.34 ± 0.58	1.38 ± 0.15	0.32 ± 0.32	1.47 ± 0.07	0.79 ± 0.53
GRV94	1.15 ± 0.77	0.33 ± 0.58	1.45 ± 0.16	0.34 ± 0.31	1.48 ± 0.08	0.88 ± 0.53

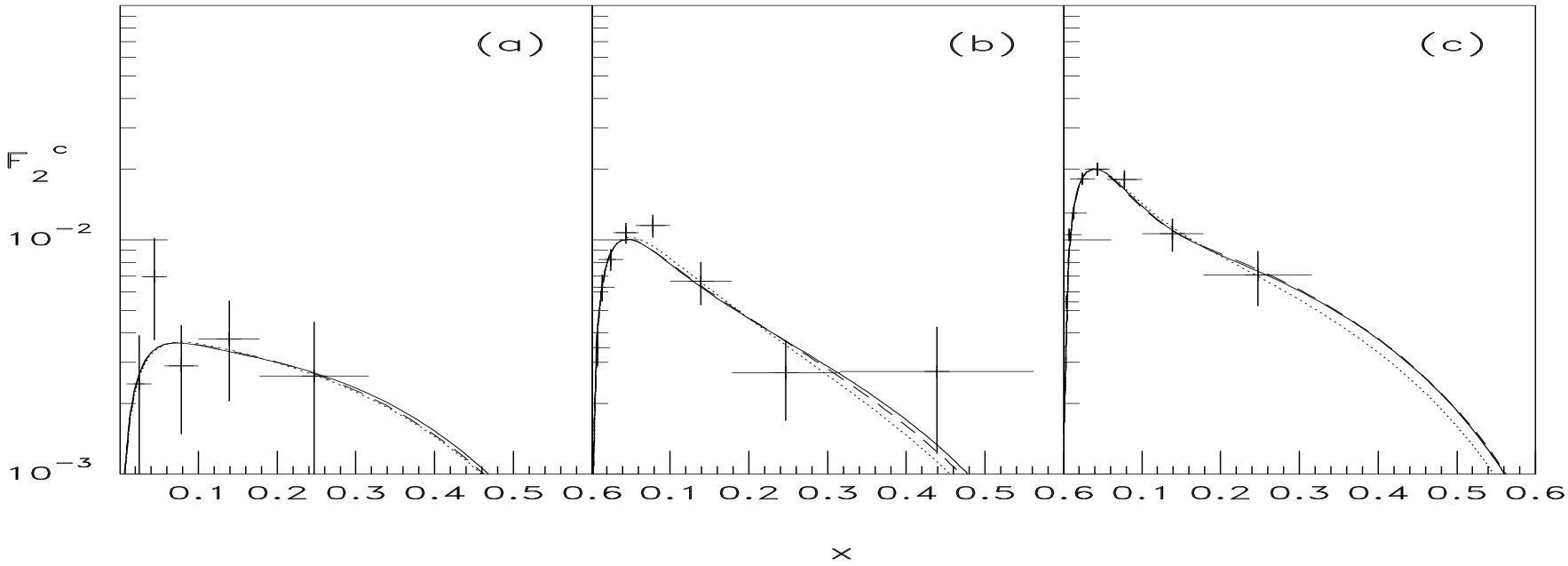

Figure 19: The sum of the EC and IC structure functions, weighted by the parameters α and β, are compared to the EMC F_2^c for $\overline{\nu} = 53$ (a), 95 (b) and 168 (c) GeV. The results are shown for CTEQ3 (solid), MRS G (dotted) and GRV98 (dashed) as a function of x. (From Harris, Smith and R.V..)

Light Cone IC Leads to Interesting Observable Consequences

IC states can either fragment, like normal leading-twist factorization of charm production or coalesce into charm mesons and baryons

Charm hadrons formed by IC coalescence are produced with much higher x_F than at leading twist, these are leading charm hadrons

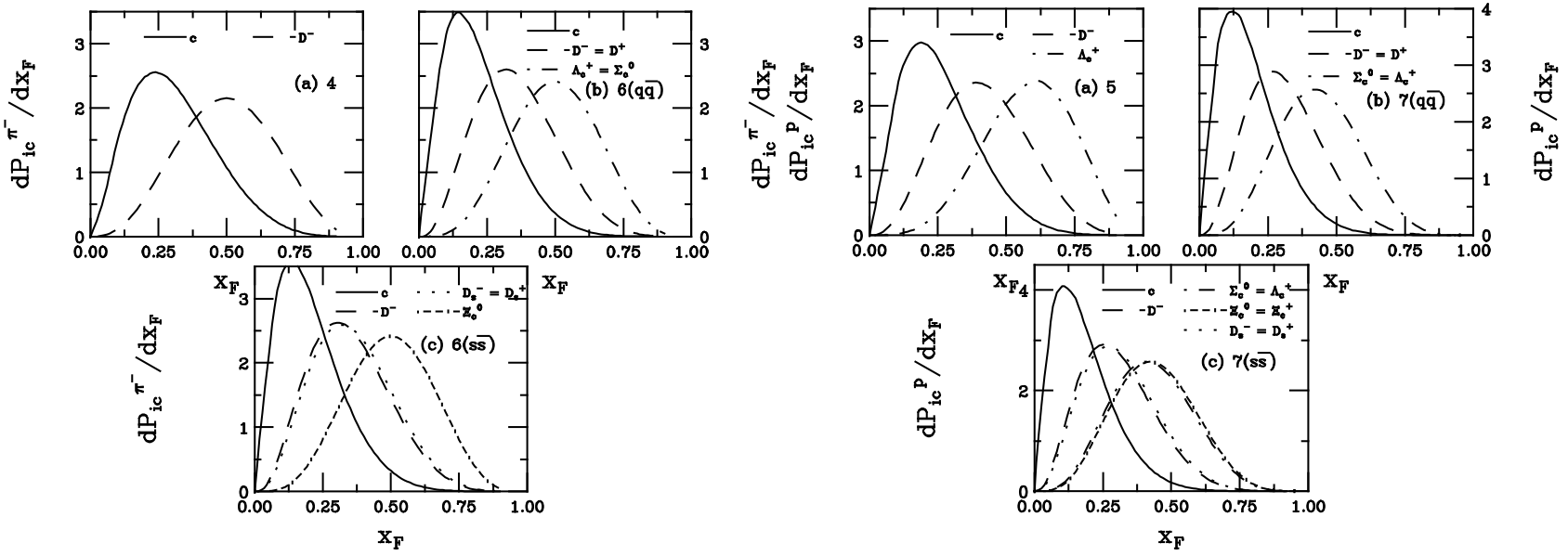

Figure 20: Charm hadron production in the intrinsic charm model with a π^- (left) and proton (right) projectile. The probability distributions, $(1/P_{\rm ic}^n)(dP_{\rm ic}^n/dx_H)$, for uncorrelated fragmentation and coalescence with a π^- projectile (left) are given for the minimal 4-particle Fock state (a) and for the 6-particle Fock states with light quarks $q = u$, d (b) and with strange quarks (c). The probability distributions, $(1/P_{\rm ic}^n)(dP_{\rm ic}^n/dx_H)$, for uncorrelated fragmentation and coalescence with a proton projectile (right) are given for the minimal 5-particle Fock state (a) and for the 7-particle Fock states with light quarks $q = u$, d (b) and with strange quarks (c). The solid curve in each case is the charm quark distribution which also serves as the hadron distribution for independent fragmentation. The other curves are the probability distributions for hadron production by coalescence, including: D^- (dashed), Λ_c^+ (dot-dashed), Ξ_c^0 (dot-dash-dashed) and D_s^- (dotted). If the shape of the probability distribution is the same for any two hadrons (such as the Σ_c^0 and the Λ_c^+ in (b)) in a configuration, it is indicated. [From Gutierrez and RV.]

Asymmetries Observed Between Leading and Nonleading Charm

Asymmetries mostly observed in fixed target $\pi^- A$ interactions

Should be observable with protons too, fewer measurements with poorer statistics

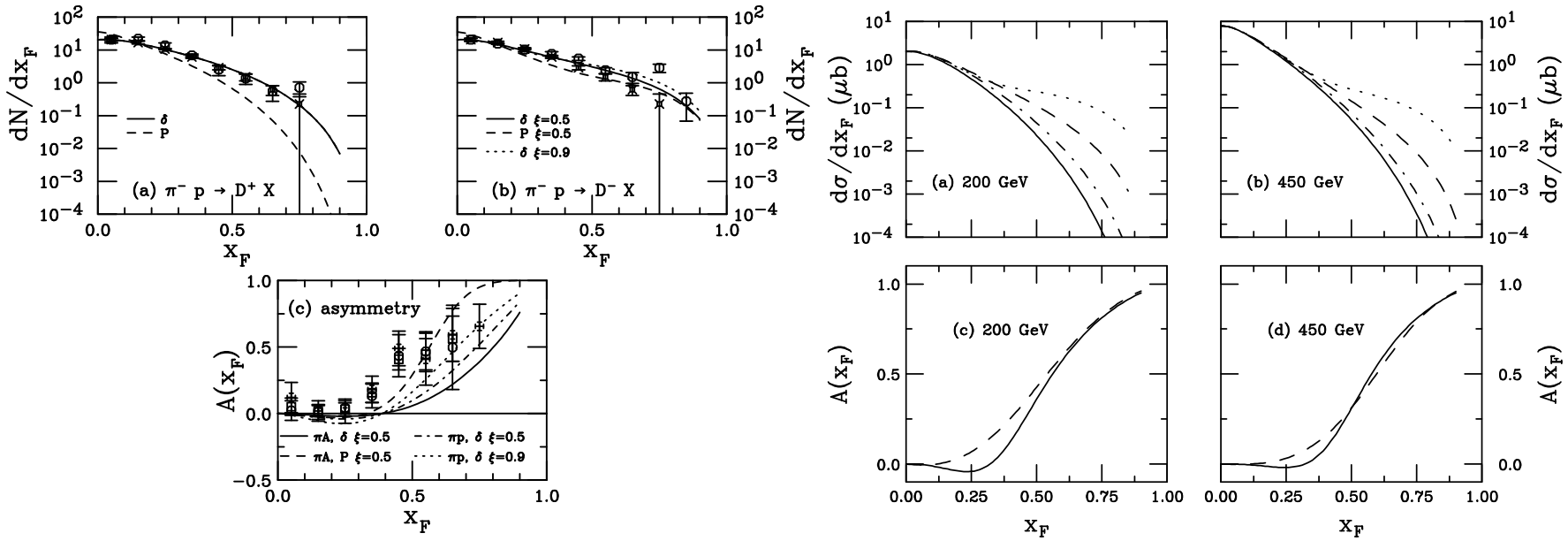

Figure 21: (Left) results for (a) nonleading charm and (b) leading charm distributions in $\pi^- p$ interactions at 340 GeV and (c) the asymmetry are compared with the WA82 (circles) and E769 (stars) data. The combined asymmetry from both experiments is also shown (squares). The calculations are with GRV LO distributions using delta-function (solid) and Peterson function (dashed) fragmentation with the intrinsic charm contributions to nonleading and leading charm production. The dotted curve in (b) shows the leading D distribution with $\xi = 0.9$ (weight factor of coalescence relative to fragmentation). The dot-dashed curve is shows the prediction of fusion with final-state coalescence. In (c), the dashed curve is calculated with the Peterson function and the solid curve with delta-function fragmentation. Both are averaged over nuclear target. The dot-dashed curve uses delta-function fragmentation and a proton target. The dotted curve shows the leading contribution calculated with $\xi = 0.9$ for a proton target. [From Brodsky and RV.] (Right) Predictions of the energy dependence of charm hadron production by a proton beam on lead targets. The curves in (a) and (b) illustrate the dependence of leading charm on the projectile energy. The fusion curve (solid) includes no IC while the other curves assume $P_{\rm ic} = 0.31\%$. They are D^- (dashed), D^+ (dot-dashed) and Λ_c (dotted). The D^-/D^+ (solid) and Λ_c/D^- (dashed) asymmetries are shown at 200 GeV (c) and 450 GeV (d).

A Dependence of Intrinsic Charm

EMC analyses of EMC charm structure function data find $P_{\rm ic} \sim 0.3 - 1$ %

Intrinsic charm is stronger at lower energies because $\sigma_{\rm lt}$ is smaller but because $\sigma_{\rm ic}$ does not change much with energy, effect decreases as energy increases

Intrinsic charm dominates the A dependence at high x_F, note difference between projectile and target regions

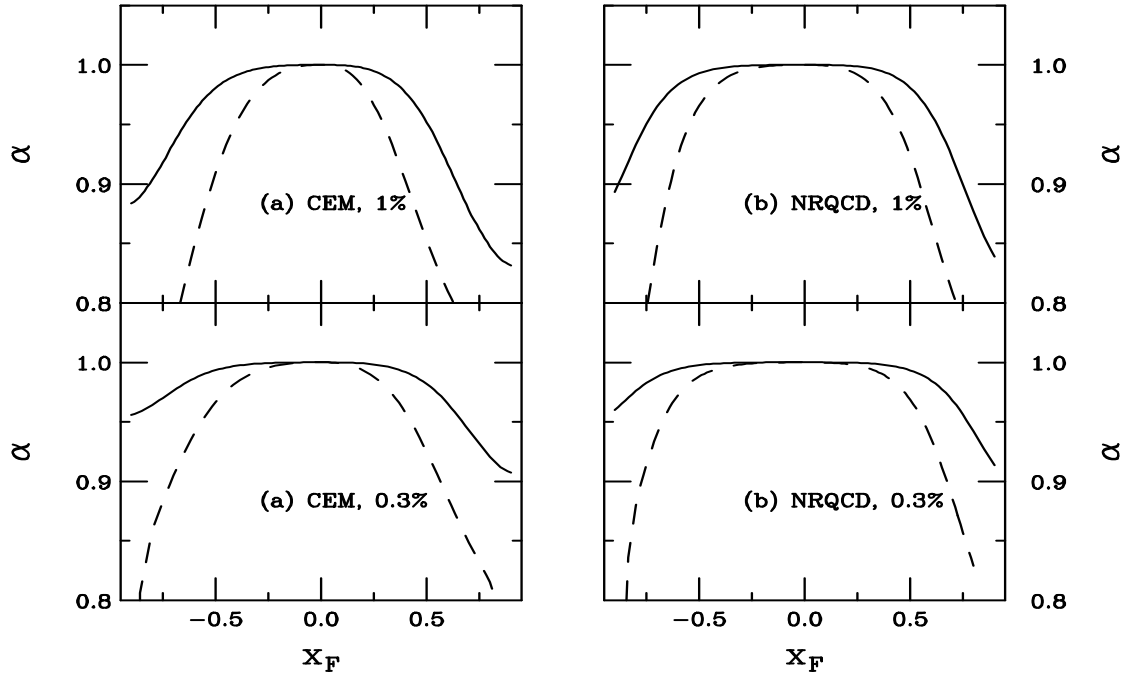

Figure 22: The A dependence of intrinsic charm at 800 GeV (solid) and 120 GeV (dashed). In (a) and (c) an effective production probability of 1% is assumed in the CEM and in NRQCD respectively while in (c) and (d) $P_{\rm ic}^{\rm eff} = 0.31\%$ is assumed in the CEM and in NRQCD. At $x_F > 0$ the projectile proton strikes a nuclear target, at negative x_F, the nuclear 'projectile' strikes a proton target, making the A dependence different in the two regions.

Nuclear Absorption

A Dependence of J/ψ and ψ' Not Identical

Extensive fixed-target data sets (NA50 at SPS, E866 at FNAL) show clear difference at midrapidity [NA50 ρL fit gives $\Delta\sigma = \sigma^{\psi'}_{\rm abs} - \sigma^{J/\psi}_{\rm abs} = 4.2 \pm 1.0$ mb at 400 GeV, 2.8 ± 0.5 mb at 450 GeV for absolute cross sections]

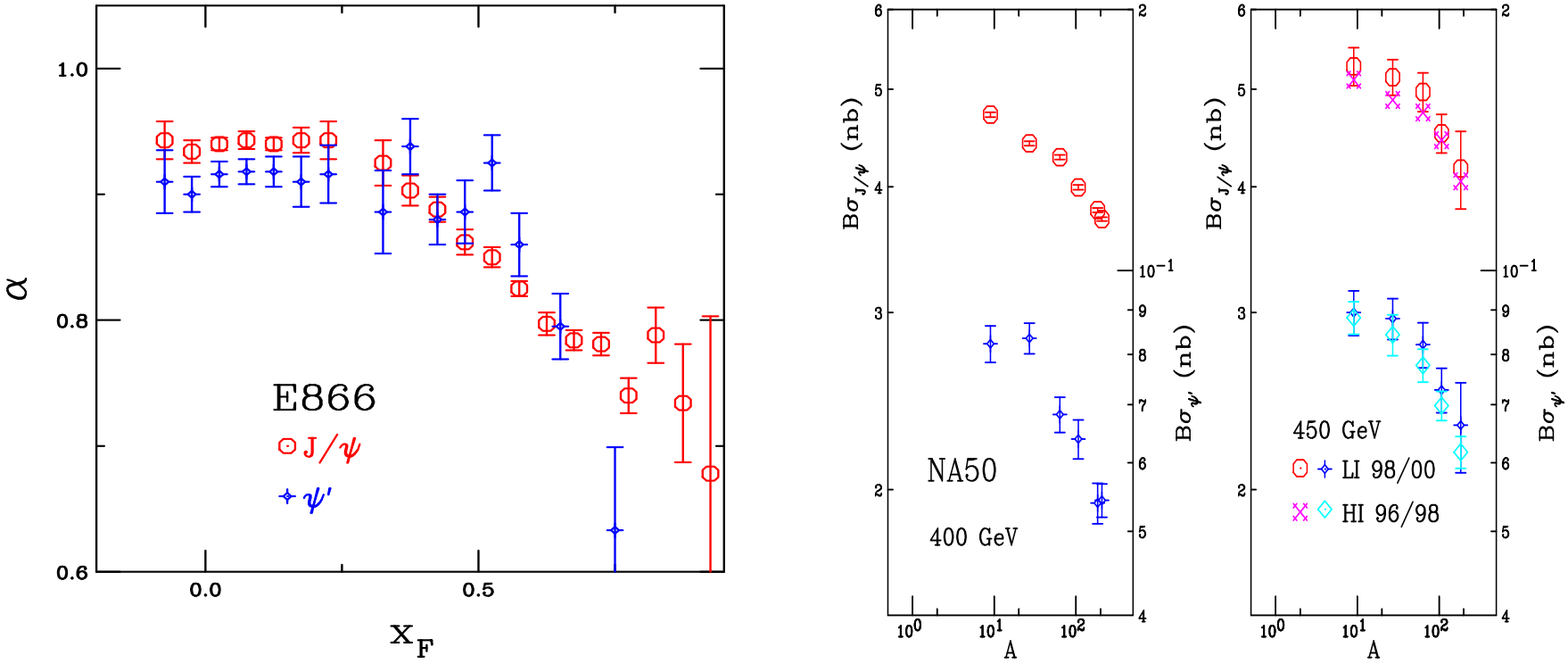

Figure 23: The J/ψ A dependence (left) as a function of x_F at FNAL ($\sqrt{S_{NN}} = 38.8$ GeV) and (right) and a function of A at the SPS (NA50 at $p_{\rm lab} = 400$ and 450 GeV) for J/ψ and ψ' production.

PHENIX Has Measured R_{dAu} for ψ' and χ_c

First results shown at Quark Matter '12 for ψ' and χ_c

$R_{\mathrm{dAu}} \sim 0.75 \pm 0.20, 0.75 \pm 0.25, 0.30 \pm 0.15$ **for J/ψ, χ_c and ψ' respectively**

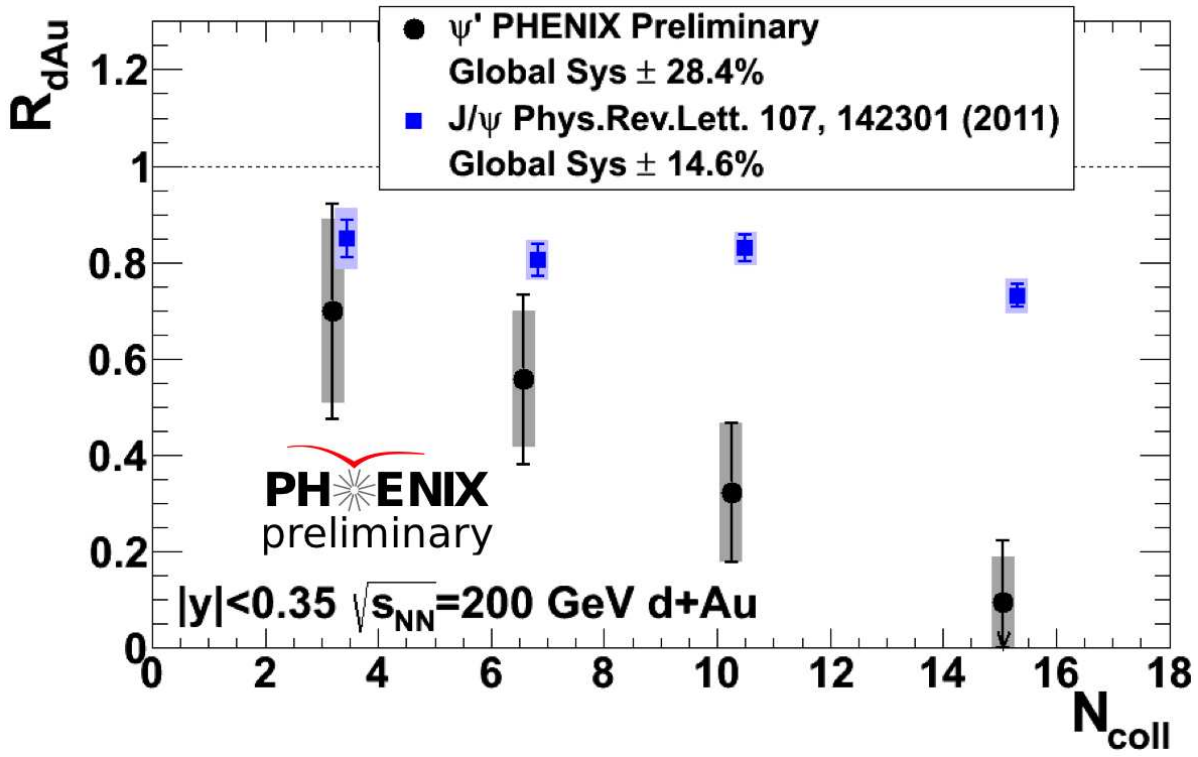

Figure 24: The J/ψ and ψ' N_{coll} dependence as reported by PHENIX at QM'12 by D. McGlinchey.

A Dependence of Charmonium States May Differ

NRQCD approach predicts different cross sections for J/ψ, ψ' and χ_c

$$\frac{d\sigma_{pA}^{\psi,\,\mathrm{tot}}}{dx_F} = \left[\frac{d\sigma_{pp}^{\psi,\,\mathrm{dir,\,oct}}}{dx_F} + \sum_{J=0}^{2} B(\chi_{cJ} \to \psi X)\frac{d\sigma_{pp}^{\chi_{cJ},\,\mathrm{oct}}}{dx_F} + B(\psi' \to \psi X)\frac{d\sigma_{pp}^{\psi',\,\mathrm{oct}}}{dx_F}\right] \int d^2b T_A^{\mathrm{eff\,(oct)}}(b)$$
$$+ \int d^2b \left[\frac{d\sigma_{pp}^{\psi,\,\mathrm{dir,\,sing}}}{dx_F} T_A^{\psi,\mathrm{dir,eff\,(sing)}}(b) + \sum_{J=0}^{2} B(\chi_{cJ} \to \psi X)\frac{d\sigma_{pp}^{\chi_{cJ},\,\mathrm{sing}}}{dx_F} T_A^{\chi_{cJ},\,\mathrm{eff\,(sing)}}(b) + B(\psi' \to \psi X)\frac{d\sigma_{pp}^{\psi',\,\mathrm{sing}}}{dx_F} T_A^{\psi',\,\mathrm{eff\,(sing)}}(b)\right]$$

$$T_A^{\mathrm{eff}}(b) = \int_{-\infty}^{\infty} dz\, \rho_A(b,z) \exp\left\{-\int_z^{\infty} dz' \rho_A(b,z')\sigma_{\mathrm{abs}}(z'-z)\right\}$$

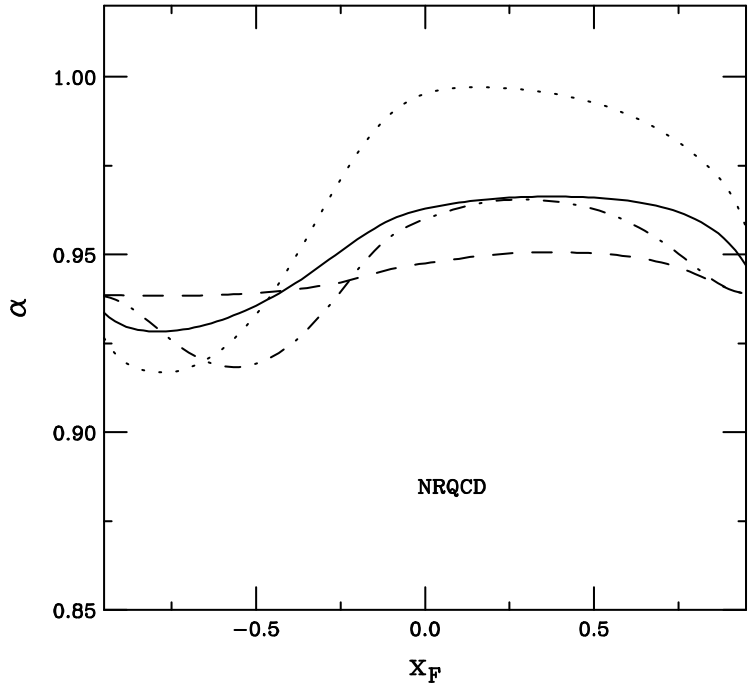

Figure 25: The A dependence of singlet and octet absorption is shown at 920 GeV. The total J/ψ dependence is given in the solid curve, the direct J/ψ in the dashed, ψ' in the dot-dashed, and χ_c in the dotted curve assuming $\sigma_{\mathrm{abs}}^{\mathrm{octet}} = 4$ mb and $\sigma_{\mathrm{abs}}^{\mathrm{singlet}\,J/\psi} = 5$ mb.

Effective Absoprtion Cross Section Energy Dependent

Once data corrected for shadowing effects, dependence of effective absorption cross section on center of mass energy is clear

In backward region, quarkonium states should be fully formed within the target

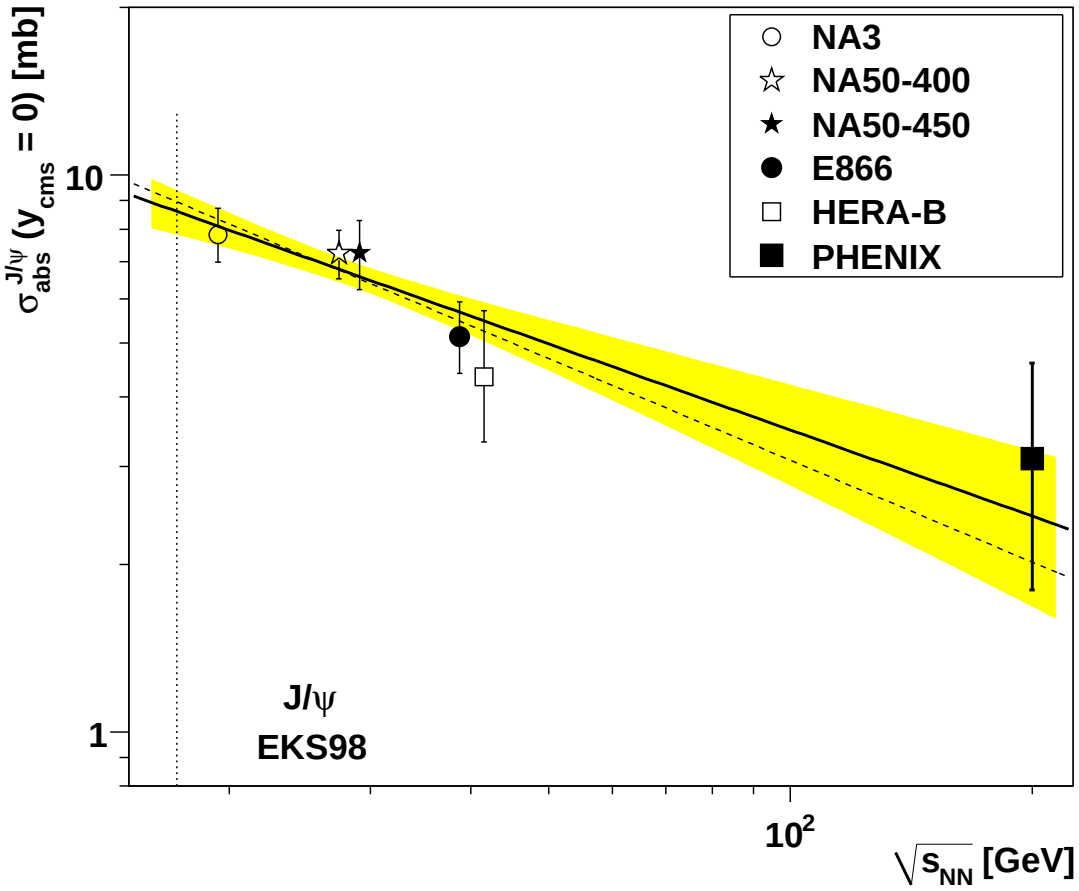

Figure 26: At midrapidity, the effective absorption cross section decreases as a function of energy. (Modified from Lourenco, Wohri and RV.)

That's Not All Folks

Υ Teaser

Υ A Dependence Also of Interest in Backward Region

E772 measured possible difference between $\Upsilon(1S)$ and $\Upsilon(2S) + \Upsilon(3S)$ A dependence in the backward x_F region

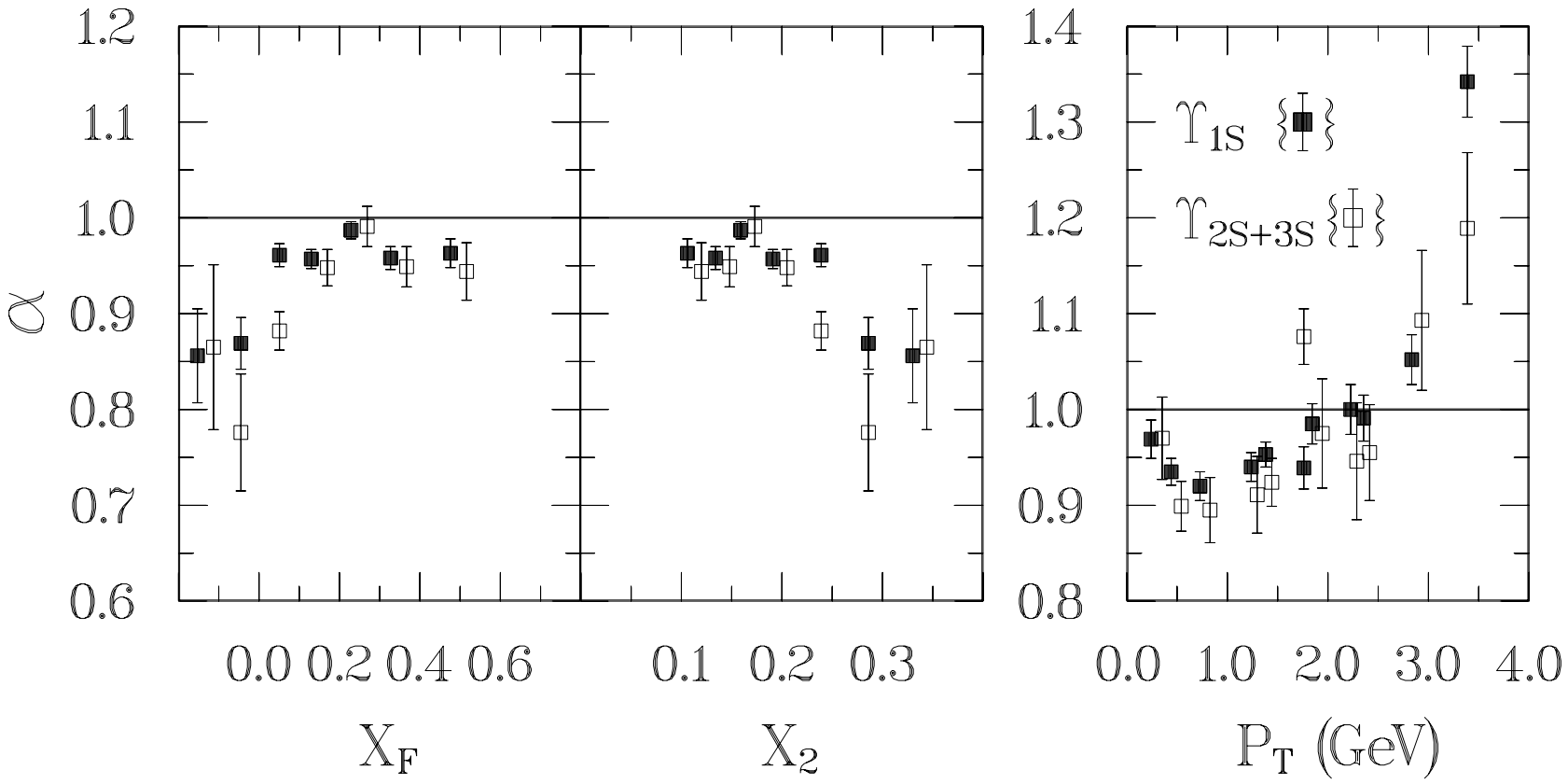

Figure 27: The E772 Υ A dependence as a function of x_F, x_2 and p_T.

Summary .

- Lots of interesting nuclear effects on open charm and charmonium
- An experiment like AFTER could sort them out